Cooperation between cortical and cytoplasmic forces shapes planar 4-cell stage embryos

Silvia Caballero-Mancebo[1*], Daniel Gonzalez Suarez[1], Janet Chenevert[1], Sameh Ben-Aicha[2], Lydia Besnardeau[1], Alex McDougall[1] and Rémi Dumollard[1,3*]

[1]Laboratoire de Biologie du Développement de Villefranche-sur-Mer, Institut de la Mer de Villefranche-sur-Mer, Sorbonne Université, CNRS, 06230 Villefranche-sur-Mer, France.
[2]Institut de Biologie de Valrose, Université Côte-d'Azur, CNRS, 03108 Nice, France.
[3] Lead contact.

* Corresponding author: remi.dumollard@imev-mer.fr, silvia.caballero@imev-mer.fr

ABSTRACT

Early embryonic cleavages often follow conserved geometric rules, resulting in species-specific cleavage patterns. How these rules are mechanistically implemented, however, varies widely across species and remains poorly understood. Here, using quantitative 3D live imaging, mechanical and biochemical manipulations, we dissect the mechanisms governing centrosomal complex (CC) migration and spindle orientation in ascidian 2-cell stage embryos, which generate the characteristic planar, square 4-cell stage. We show that following the first mitotic division, the CCs in each blastomere form at variable orientations relative to the mother spindle and progressively achieve parallel and coplanar alignment during interphase of the 2-cell stage. Final CC orientation is established before nuclear envelope breakdown, contrasting with the dynamic spindle reorientation during mitosis reported in other organisms. Our analyses reveal that CC rotation is driven by forces acting on long astral microtubules and guided by an anisotropic, endoplasmic reticulum (ER)-rich domain that surrounds the CCs. This ER domain is associated with a dense astral microtubule network, enabling efficient length-dependent microtubule pulling that can orient the CCs even in the absence of cell shape cues. In parallel, dynein-mediated cortical pulling refines CCs tilt and maintains coplanarity. Together, these findings uncover a cell-cycle-regulated cooperation between ER-mediated cytoplasmic forces and anisotropic cortical forces that ensures robust planar cleavage in ascidian early embryos.

INTRODUCTION

Species-specific patterns of early cleavage divisions have fascinated developmental biologists for more than a century. Despite the diversity of embryo sizes and shapes, early cleavages typically follow two conserved geometric principles: Hertwig's rule, which states that the mitotic spindle aligns along the longest axis of the cell (Hertwig, 1884), and Sachs' rule, where division occurs at right angles to the previous one (Sachs, 1877). These rules collectively explain the widespread emergence of the planar and square arrangement of blastomeres at the 4-cell stage, a configuration observed across a broad spectrum of animal taxa (Caballero-Mancebo et al., 2026; McDougall et al., 2019; Pierre et al., 2016). Yet, despite the apparent universality of these geometric rules, the mechanisms by which they are implemented are species-dependent and remain the subject of active investigation and debate.

The physical environment of the embryo can impose significant constraints on blastomere arrangement and cleavage orientation. Nematode embryos, encased in a rigid eggshell, display a striking diversity of 4-cell stage morphologies, ranging from square to linear configurations, depending on the mechanical properties and the aspect ratio of the eggshell (Giammona and Campàs, 2021; Schulze and Schierenberg, 2011; Seirin-Lee et al., 2022). In contrast, unconfined embryos and embryos with a non-restrictive confinement, such as ascidian and echinoderm embryos, more consistently exhibit the archetypal flat, square 4-cell configuration (Minc and Piel, 2012; Pierre et al., 2016). However, this configuration is far from the mechanically stable configuration of 4 blastomeres—a tetrahedron—but arises due to the short division times of early embryos (Giammona and Campàs, 2021), suggesting that oriented cell divisions underpin the flat and square shape of 4-cell stage embryos.

To generate a symmetric and flat 4-cell stage embryo, the first two cell divisions must be equal and at 90° to each other, and the mitotic spindles of each cell of the 2-cell stage embryo must be coplanar and parallel. In large cells like the blastomeres of *Xenopus* embryos, geometric constraints coupled to yolk stratification are sufficient to generate flat 4-cell stage embryos (Pierre et al., 2016a; Wühr et al., 2010). This model postulates simply that cytoplasmic pulling forces acting on astral microtubules must be proportional to their lengths (Kimura and Kimura, 2011a; Pierre et al., 2016). This is thought to be achieved by dynein-dependent pulling of cytoplasmic cargoes moving towards the minus end of microtubules. However, the nature of these cargoes remains to be established (Xie et al., 2022).

In smaller cells, dynein-dependent cortical pulling forces become more prominent. In cultured cells and in cells of the *Drosophila* notum epithelium, cortical pulling forces have been shown to be essential in aligning the spindle with the long axis of the interphasic cell (Anjur-Dietrich et al., 2024; Bosveld et al., 2016). Moreover, in the *Caenorhabditis elegans* early embryo, where cytoplasmic pulling and cortical pulling or pushing have all been hypothesized to play a role in spindle orientation (Bondaz et al., 2019; Grill et al., 2001; Grill and Hyman, 2005; Kimura and Kimura, 2011b; Middelkoop et al., 2024; Wu et al., 2024), cortical pulling has been shown to be essential in the alignment of the spindle to the long axis of the zygote (Wu et al., 2024) as well as to the short axis of the AB cell at the 2-cell stage, thus having an opposing action to the length-dependent cytoplasmic pulling forces exerted on astral microtubules (Middelkoop et al., 2024). Overall, these observations argue for a size-dependent mechanism to orient spindles, where large cells rely on cytoplasmic pulling forces, whereas in small cells, cortical pulling forces dominate, and point to the intriguing possibility of intermediate-sized cells integrating both mechanisms to implement stereotyped oriented cell divisions.

In this study, we analyze the centrosome and spindle movements underlying the flat and square shape of the ascidian *Phallusia mammillata* 4-cell stage embryos, which are of intermediate size between the large *Xenopus* blastomeres and the small ones of nematode embryos. We find that centrosomal complexes (CCs) align progressively with the long axis of the blastomeres during interphase when cortical pulling is strong. Laser ablation experiments reveal that the force for the orientation of CCs relies on cytoplasmic pulling of microtubules on the stratified endoplasmic reticulum (ER). Finally, we find that interfering with the balance between cortical and cytoplasmic pulling forces transforms planar 4-cell stage embryos into non-planar or non-square embryos, highlighting that a finely tuned interplay between cytoplasmic and cortical pulling controls the precise positioning of spindles and the cleavage pattern of early embryos of intermediate size.

RESULTS

Progressive parallel and coplanar alignment of the two centrosomal complexes at the 2-cell stage

In order to follow the movements of each centrosome of the centrosomal complexes (CCs) during the 2-cell stage, we performed 3D live imaging of embryos injected with EB3-3xVenus to label the centrosomes from mitosis of 1-cell stage to the beginning of cytokinesis of the 2-cell stage (Fig. 1A, movie 1). In the vegetal view, two distinct centrosomes can be observed at each pole of the spindle at anaphase of the 1-cell stage, coinciding with the beginning of cytokinesis of the first mitosis (Fig. 1A-inset, t = 2 min). We found that the CCs in the two forming daughter cells are not initially parallel to each other (in 60% of all analyzed embryos) and progressively align with each other during the interphase of the 2-cell stage. This alignment results in two parallel CCs at nuclear envelope breakdown (NEB) of the 2-cell stage (Fig. 1A, 16-20 min), which in turn gives rise to two parallel spindles at metaphase of the 2-cell stage (Fig. 1A, 20-26 min). To generate the characteristic flat and square geometry of the ascidian 4-cell stage embryo, the two spindles at the 2-cell stage must not only be parallel but also coplanar; a side view revealed that, indeed, the two CCs remain largely coplanar throughout CCs migration at the 2-cell stage (Fig. 1A, bottom row).

To further document the migration pattern of CCs and how they orient over time, we tracked the position of the anterior and posterior centrosomes within each CC in 3D (Fig. 1B) and measured the rotation and tilt angles of the segment formed by the centrosomes of each CC with respect to the mitotic spindle at 1-cell stage (Fig. 1C-D, S1A). We found that initially the CCs form with at a rotation angle of 68.2° ± 24.6 with respect to the mother spindle, and that during interphase of the 2-cell stage, the CCs rotate to achieve a final angle of 82.5° ± 5.3 with respect to the mitotic spindle at the 1-cell stage by the time the daughter cells are in metaphase of the 2-cell stage. Surprisingly, this final position of the CCs does not change much from the time of NEB, contrary to what has been observed in other embryos and somatic cells, where the final position of the spindle is fine-tuned during metaphase and anaphase (Anjur-Dietrich et al., 2024; Bondaz et al., 2019; Gönczy et al., 2001; Grill and Hyman, 2005), suggesting that spindle positioning in ascidian embryos is largely predetermined before NEB rather than dynamically adjusted during mitosis.

Consistent with this idea, the tilt angle between the CCs and the 1-cell stage spindle also decreased from 25.5° ± 22.4 to 15.1° ± 11.1 (Fig. 1D) and did not converge to zero. This observation is in agreement with previous reports describing a posterior-vegetal tilt of the spindle in ascidians at the 8-

cell stage (Negishi et al., 2007). Comparing the orientation of the sister CCs and spindles at the 2-cell stage further confirmed our observations that they progressively become parallel, as indicated by a reduction in the rotation angle between them from 48.4° ± 25 to 6.6° ± 5.5 (Fig. 1E, S1B - Rotation), and that they are mostly coplanar throughout CC migration, as reflected by the small change in the tilt angle between them from 3.9° ± 4.8 to 1.8° ± 3.1 (Fig. 1E, S1B - Tilt). Altogether, this analysis revealed that the proper orientation of the CCs required to generate a flat, square 4-cell stage ascidian embryo is progressively established during the end of mitosis of the 1-cell stage and interphase of the 2-cell stage, and that by the time of mitotic entry at 2-cell stage, the final position of the future spindle is already defined.

To better understand the mechanisms that orient the CCs, we examined their migration at a higher spatiotemporal resolution (Fig. 2A, movie 2). We found that the CCs form in the center of the daughter cell at some distance from the nucleus (~17 µm) before the first cleavage is complete (Fig. 2A, 30 s, arrowhead), and that the centrosomes within each CC remain close to each other and move together until the end of interphase of the 2-cell stage, when the centrosomes in each CC start to separate from each other and the nucleus positions between them (Fig. 2A-B, 12- 14 min) right before NEB. Interestingly, the CCs have already reached their final orientation before their centrosomes start separating (Fig. 1D-E, 2B), indicating that the final orientation of the CCs is achieved without centrosome separation. Since the centrosomes within a CC remain close together during their migration, we asked whether a physical link between them is necessary for their proper migration. To that end, we performed periodic laser ablations every 90 s between the two centrosomes in one of the two sister CCs from the time when both centrosomes were identifiable (late anaphase of the 1-cell stage) until the nucleus reached the CC center (Fig. 2C, movie 3). We found that neither the rotation nor the tilt angles were affected when centrosomes were ectopically separated by laser ablations (Fig. 2C', S2A-B), and that the ablated 2-cell stage embryos still divided into flat and square 4-cell stage embryos.

Because centrosome separation initiates when the nucleus reaches them, we assessed whether the CCs use the nuclei to orient/power their movements as previously observed in *C. elegans* and *Drosophila* embryos (Bondaz et al., 2019; Buttrick et al., 2008; Meyerzon et al., 2009; Tanenbaum and Medema, 2010). To test this possibility, we performed periodic laser ablations every 90 s between the CC and the nucleus in one of the two cells from the time when both centrosomes were identifiable until the nuclei reached the center of the CC (Fig. 2D, movie 4). We found that these ablations impaired nucleus migration (Fig. S2C) but did not affect either CC movements or their final orientation (Fig. 2D', S2D), as the CCs in sister cells of ablated embryos eventually became parallel and coplanar as in control embryos.

Altogether, these results show that CCs movements initiate at late anaphase of mitosis I and proceed during cytokinesis and interphase of the 2-cell stage in ascidians. These movements do not rely on mechanisms previously described in other embryos, such as *Xenopus* embryos (Wühr et al., 2010), *C. elegans* zygotes (Meyerzon et al., 2009), or *Drosophila* blastoderm embryos (Buttrick et al., 2008; Wong et al., 2024), and they are not supported by either the nuclei or antiparallel microtubule sliding between centrosomes.

179 **CC movements are powered by forces generated by astral microtubules**
180 As the aforementioned mechanisms do not appear to contribute to CC movements, we considered the
181 astral microtubule network to be the most likely source of the forces driving CC migration. We analyzed
182 microtubule distribution at key times during CC migration and found that the network of astral
183 microtubules grows at anaphase of the first mitosis and expands into the whole volume of the cell
184 during interphase of the 2-cell stage before sharply retracting at prophase (Fig. 3A). To understand
185 how network remodeling could contribute to the migration of the CCs, we analyzed the density of
186 microtubules from the centrosome to the cell cortex. We found that in interphase (Fig. 3A'), a dense
187 network of microtubules is formed extending from the centrosomes across the central cytoplasm (Fig.
188 3A', blue shaded area), surrounded by a less dense peripheral network of microtubules near the cortex
189 (Fig. 3A', red shaded area). Upon mitotic entry at the 2-cell stage, this organization was lost, and the
190 microtubule network became restricted to the pericentrosomal region, with the peripheral population
191 markedly diminished (Fig. 3A''). The long astral microtubules observed during interphase may be the
192 sites of force generation to move the CCs either by cytoplasmic pulling, as demonstrated in sea urchin
193 embryos (Minc et al., 2011; Minc and Piel, 2012), or by pulling of astral microtubules on the cell cortex
194 previously shown in ascidian zygotes (Rosfelter et al., 2024), or both. To test the involvement of astral
195 microtubules in the orientation of the CCs, we performed periodic laser ablations (every 90 s) of astral
196 microtubules in one of the two sister cells (Fig. 3B, movie 5) from the time when both centrosomes in
197 each CC were identifiable (late anaphase of the 1-cell stage) until NEB of the 2-cell stage. We found
198 that the rotation angle of the CCs was severely affected in the ablated cell but not in the non-ablated
199 one (Fig. 3B'), and that the sister CCs, and thus the sister spindles, at the 2-cell stage were no longer
200 parallel (Fig. S3A – Rotation Ablated). In contrast, the tilt angle was not affected by these laser ablations
201 (Fig. 3B'), and the CCs and spindles remained coplanar (Fig. S3A – Tilt Ablated). To confirm these
202 observations, we interfered with astral microtubules using the drug 2-methoxyestradiol (2ME), which
203 preferentially affects dynamic microtubules without impairing spindle formation (Kamath et al., 2006)
204 (Fig. 3C). Incubating zygotes at anaphase of the 1-cell stage with 2ME drastically reduced the size of
205 centrosomal asters during interphase of the 2-cell stage (Fig. 3C) and prevented CC migration, leading
206 to strong defects in both rotation and tilt angles of the spindles at the end of 2-cell stage and resulting
207 in a loss of coplanarity (Fig. 3C'-C'', S3B-B').
208
209 Altogether, these results demonstrate that forces exerted on astral microtubules are responsible for
210 the proper migration and orientation of the CCs, and thus the spindles, in 2-cell stage ascidian embryos.
211 In other systems, these forces are generated by dynein motors either anchored at the plasma
212 membrane, which exert tension on astral microtubules as they move toward their minus ends (Anjur-
213 Dietrich et al., 2024; Kiyomitsu, 2019; Laan et al., 2012; Omer et al., 2018), or bound to intracellular
214 organelles such as the ER or endosomes (Cheng and Ferrell, 2019; Shamipour et al., 2021; Woźniak et
215 al., 2009). To explore the contribution of these mechanisms to the shaping of planar ascidian 4-cell
216 stage embryos, we sought to localize intracellular dynein by immunocytochemistry against the dynein
217 co-factor, dynactin. Using ascidian-specific anti-dynactin antibody (Fig. 3D, S3C), we found that
218 dynactin is enriched both in the pericentrosomal cytoplasm and at the cell cortex. These two pools of
219 dynactin closely correlate with the dense central and the peripheral microtubule populations,
220 respectively, observed in interphase cells (Fig. 3A, A').
221

222 Together, these findings suggest that dynein–dynactin complexes are enriched on locations supporting
223 a role for both cytoplasmic and cortical pulling in the positioning of CCs and spindles. We then sought
224 to discriminate the role of each mechanism in the positioning of the CCs.
225
226 **An anisotropic ER domain may drive CC movements in the ascidian embryo.**
227 Recent work indicates that the cytoplasm of ascidian embryos is a dense mixture of yolk granules and
228 organelles (Stoev et al., 2025) and that the interaction between cytoskeletal structures and
229 cytoplasmic components generates forces that shape the embryo and drive cytoplasmic organizations
230 (Caballero-Mancebo et al., 2024). Moreover, previous studies have shown that the ER is transported
231 by dynein motors and is able to generate pulling forces on astral microtubules (Lane and Allan, 1999;
232 Mukherjee et al., 2020; Woźniak et al., 2009). In ascidian embryos, the ER and yolk granules segregate
233 in the cytoplasm with the ER accumulating around the sperm aster in the zygote, while yolk vesicles
234 are excluded from the pericentrosomal region (Rosfelter et al., 2024). We thus asked if the ER could
235 serve as the guiding cue for the CCs to orient. We first analyzed the distribution of ER over time and
236 found that the mitotic spindle at the 1-cell stage and the CCs during the 2-cell stage were surrounded
237 by an accumulation of ER (Fig. 4A, S4A, movie 6), closely resembling both the pericentrosomal dense
238 astral microtubule population and the localization of dynactin (Fig. 3A, D, and S4A). Segmentation and
239 morphometric analysis of these ER domains revealed that, unlike the roughly spherical shape of the
240 cell (0.85 ± 0.05 sphericity during interphase), the ER forms a cytoplasmic domain with an ellipsoid
241 shape (0.62 ± 0.04 sphericity) and a clearly defined long axis (Fig. 4B).
242
243 The observed enrichment of dynactin and ER over time around the CCs points to the possibility of the
244 CCs leveraging the anisotropic shape of the ER domain to align with its long axis, as predicted by length-
245 dependent pulling on microtubules to position asters and spindles (Kimura and Kimura, 2011b), even
246 in the absence of a geometrically defined long axis of the cell. To address this hypothesis, we quantified
247 the relative alignment between the long axes of the ER domain and the cell, and the CCs using
248 bootstrap statistics (Fig. 4C). We found that initially, the long axes of the cell, ER, and the CCs are not
249 aligned to each other (Fig. 4C – 2 min, 4D – 2 min), displaying random orientations, which result in an
250 average angle of ~45°. As cytokinesis and interphase progress, the angle between the long axes of ER
251 and the CCs gradually decreases, indicating progressive alignment between them before becoming
252 parallel at the end of interphase (Fig. 4C – 12 min, green; 4D – 12 min, green and grey). In contrast,
253 neither the long axis of the ER domain nor that of the CCs aligns with the long axis of the cell over the
254 same period (Fig. 4C), suggesting that cell shape does not provide a dominant geometrical cue for CC
255 orientation. Interestingly, at NEB, coinciding with the shortening of astral microtubules, the ER and the
256 CCs become momentarily misaligned (Fig. 4C – 17 min, 4D – 17 min), before realigning with the cell's
257 long axis during mitosis of the 2-cell stage. Together, this analysis reveals that the shape of the cell
258 does not provide a consistent geometrical cue for CC orientation, and suggests that, instead, the ER
259 acts as a cytoplasmic scaffold that guides CC alignment independently of cell geometry, even though
260 the final orientation of the spindles at the 2-cell stage obeys the Hertwig rule (Dumollard et al., 2017).
261
262 Even though the shape of the 2-cell stage blastomeres remained fairly spherical, a long axis may still
263 be sensed by microtubules to position the CCs and spindles. To further test whether the ER–CC
264 alignment depends on external cell geometry or arises intrinsically from cytoplasmic organization, we
265 cultured the embryos in calcium and magnesium-free seawater (CMF) to remove the contribution of
266 cell adhesion to cell shape (Fig. 4E-F, movie 7). The blastomeres of CMF-treated embryos remained

267 almost perfectly spherical, displaying an average sphericity of 0.96 ± 0.04 (Fig. 4G). The rotation angle
268 between the CCs at the 2-cell stage relative to the mitotic spindle of the 1-cell stage, however, was
269 significantly altered, whereas the tilt angle remained unaffected (Fig. 4E'–E''). The defective rotation
270 of the CCs at the end of the 2-cell stage prevented the mitotic spindles from being parallel at mitosis
271 (Fig. S4B-C) and affected the characteristic square geometry of 4-cell stage embryos. Planarity of the
272 embryos was, however, preserved in CMF-treated embryos (Fig. S4B-C). We then analyzed the shape
273 of the ER domain around the CCs in CMF-treated embryos (Fig. 4F) and found that it was less ellipsoidal
274 than in control embryos - average sphericity of 0.91 ± 0.04 (Fig. 4G) - supporting the idea that the ER
275 can mirror the cell shape anisotropy. Moreover, we found that the angle between the long axis of the
276 ER and the CCs was consistently higher than in control embryos, indicating reduced alignment between
277 them (Fig. 4H). This suggests that cell geometry primarily impacts the progressive alignment of the CCs
278 through rotation by cytoplasmic-generated forces, whereas the tilt angle does not seem to be
279 influenced by cell shape.
280
281 **Anisotropic cortical pulling forces maintain the CCs coplanar during CCs migration**
282 We next asked if cortical pulling forces control the posterior tilt along the anterior-posterior axis (Fig.
283 1A, D). To that end, we first monitored the evolution of cortical pulling forces during CC migration by
284 imaging plasma membrane invaginations towards the centrosomes after cortical softening with 1
285 µg/ml Latrunculin B (Fig. 5A-B, movie 8), an indication of cortical pulling sites (Godard et al., 2021;
286 Rosfelter et al., 2024). We found that plasma membrane invaginations appear at anaphase of the 1-
287 cell stage and that their frequency increases during interphase of the 2-cell stage before sharply
288 decreasing at prophase and metaphase of the 2-cell stage mitosis (Fig. 5B'), similarly to what has been
289 found in the zygote (Rosfelter et al., 2024). These observations show a good temporal correlation
290 between the appearance of the network of long astral microtubules and the occurrence of cortical
291 pulling, supporting the idea that cortical pulling may also be responsible for CC movements. We then
292 looked at the spatial distribution of cortical pulling sites and found that membrane invaginations were
293 more frequent at the posterior pole of the embryo compared to the anterior pole (Fig. S5A). This
294 difference was consistent throughout the migration of the CCs and persisted until anaphase at the 2-
295 cell stage, supporting our hypothesis that asymmetrical cortical pulling forces may play a central role
296 in regulating the tilt angle and coplanarity of CCs, thereby controlling the planar architecture of the 4-
297 cell stage embryo. Surprisingly, analysis of the CCs orientation in Latrunculin B-treated embryos (Fig.
298 S5B) showed that neither rotation nor tilt angles are affected by drastic softening of the embryo cortex
299 (Fig. S5B') and that the spindles at mitosis of the putative 2-cell stage remain parallel and coplanar (Fig.
300 S5B''). This is consistent with previous reports that reducing actomyosin contractility has minimal
301 impact on sperm aster positioning (Rosfelter et al., 2024) or early spindle orientation (Berends et al.,
302 2013), and that cortical pulling can persist when actin integrity is compromised (Redemann et al.,
303 2010), while excessive cortical tension can suppress pulling (Kelkar et al., 2022). Thus, the question
304 remains as to whether cortical pulling can regulate CCs movements.
305
306 The observation of the posterior bias in cortical pulling forces and its correlation with spindle tilt led
307 us to hypothesize that increasing cortical pulling would affect CC orientation (Middelkoop et al., 2024)
308 and perturb the coplanarity of the 4-cell stage embryos. In animal cells, cortical pulling forces are
309 mediated by dynein–NuMA–LGN–Gαi complexes anchored to the plasma membrane (Anjur-Dietrich
310 et al., 2024). In this complex, the heterotrimeric G-protein subunit Gαi recruits LGN to the cortex,
311 which in turn binds NuMA that acts as a scaffold linking the cortical complex to astral microtubules,

312 thereby allowing dynein motors to generate pulling forces as they move toward the microtubule minus
313 ends. To test whether increasing cortical pulling alters CCs positioning and embryo geometry, we
314 overexpressed NuMA and targeted it to the cortex by fusing it to a pleckstrin homology (PH) domain,
315 which promotes membrane localization (Dumollard et al., 2017). In embryos expressing PH-NuMA, the
316 fusion protein predominantly accumulated at the posterior cortex (Fig. 5C, bottom row, 0 min; movie
317 9), consistent with the accumulation of plasma membrane in the posterior part of the embryo (Carroll
318 et al., 2003). The cortical pulling assay in these embryos confirmed a global increase in the number of
319 plasma membrane invaginations (Fig. 5C', Total) compared to control embryos (Fig. 5B'), with a higher
320 frequency of posterior pulling sites, confirming that cortical pulling was strengthened and correlated
321 with the accumulation of PH-NuMA.
322
323 Analysis of the orientation of CCs in embryos overexpressing cortical NuMA showed an increase in the
324 tilt angle at the 2-cell stage relative to the spindle at the 1-cell stage, while rotation remained
325 unaffected (Fig. 5D-D'', movie 10). The tilt angle was also increased between sister CCs at the 2-cell
326 stage (Fig. S5C, S5D - Tilt), which are not coplanar anymore, resulting in embryos adopting a more
327 tetrahedral configuration (Fig. 5C, 26 min), in contrast to the planar geometry observed in controls.
328 Altogether, these results suggest a model in which proper CC orientation, and thus spindle, determines
329 the planar 4-cell embryo geometry through a finely tuned balance between cortical and cytoplasmic
330 dynein-mediated pulling forces acting on astral microtubules in a cell cycle-dependent manner (Fig.
331 5E).
332
333
334 **DISCUSSION**
335 Our study uncovers the mechanisms that drive the dynamic migration of centrosomal complexes (CCs)
336 to achieve proper spindle orientation in early ascidian embryos and identifies a previously
337 underappreciated balance between cortical and cytoplasmic forces as a key determinant of embryo
338 geometry. Through quantitative live imaging and biophysical manipulations, we reveal that ascidian
339 embryos rely on a finely tuned interplay between dynein-dependent forces acting from the cell cortex
340 and cytoplasmic forces that are most likely transmitted through the ER. We demonstrate that the CCs
341 of the two cells initially form at varying angles relative to the position of the first mitotic spindle and
342 progressively achieve parallel alignment during interphase of the 2-cell stage. Interestingly, a second
343 cue determined by cortical pulling forces controls the coplanarity of the CCs, ensuring the planar
344 arrangement of the blastomeres at the 4-cell stage.
345
346 Previous studies in *C. elegans* zygotes have revealed the major role of cortical pulling forces in
347 powering centrosome separation, which is then buffered by cytoplasmic pulling forces acting on the
348 nuclear envelope (De Simone et al., 2016). However, centrosomes of enucleated 2-cell stage *C. elegans*
349 embryos can separate normally without interacting with a nucleus (Fujii et al., 2023), supporting the
350 primary role of cortical pulling forces in centrosome separation. In large cells such as *Xenopus* and
351 zebrafish eggs, however, astral microtubules cannot extend completely to the cell cortex, rendering
352 cortical pulling inefficient for centrosome separation and orientation (Pierre et al., 2016; Wühr et al.,
353 2010). In these cells, length-dependent cytoplasmic pulling forces are responsible for moving and
354 orienting centrosomes, relying on spatial cues arising from the anisotropic shape of asters sensitive to
355 both cell shape and cytoplasmic stratification (Pierre et al., 2016). In *Xenopus* embryos, final
356 positioning of the centrosomes is achieved before the nuclear envelope reforms, during anaphase of

mitosis I, via kinesin Eg5-mediated antiparallel sliding of microtubules, which separates centrosomes (Wühr et al., 2010). In *C. elegans* embryos, Eg5 activity also cooperates with cytoplasmic pulling for centrosome separation (Bondaz et al., 2019). Our laser ablation experiments show that, in ascidian embryos, neither antiparallel forces between centrosomes nor the link with the nucleus are required for the alignment of the CCs at the 2-cell stage. This finding demonstrates that ascidian embryos employ a distinct mechanism for spindle orientation that is largely independent of the nuclear or centrosomal cues that are crucial in *Xenopus* and *C. elegans*.

Ascidian embryos are of an intermediate cell size between small nematode embryos, where cortical forces dominate, and the large *Xenopus* and zebrafish embryos, where cytoplasmic forces dictate spindle orientation. Our study reveals that the final orientation of CCs and spindles depends on pulling forces on astral microtubules from both the cortex and the cytoplasm and that their balance dictates the final shape of the 4-cell stage embryo. We show that the final orientation of the CCs is achieved progressively during cytokinesis of mitosis I and interphase of the 2-cell stage, and remains unchanged during subsequent mitosis. Concomitant with this alignment, the ER accumulates progressively around the CCs, suggesting that it is pulled towards the minus ends of microtubules. This observation, together with the fact that the microtubule network is denser in areas filled with ER and devoid of yolk platelets, leads us to propose a model in which the ER is the cytoplasmic cargo supporting length-dependent microtubule pulling (Mukherjee et al., 2020; Xie et al., 2022). Microtubule exclusion from yolk-dense regions has been found in *Xenopus* to be responsible for the geometric control of cell divisions in early embryos (Pierre et al., 2016; Wühr et al., 2010). The spatial organization of the ER provides experimental evidence that the information from cell shape is robustly transmitted to the CCs by the ER domain and powered by length-dependent pulling on the ER along astral microtubules. Therefore, a stratified cytoplasm can shape where and how intracellular forces are generated, which in turn influences spindle behavior (Pierre et al., 2016) and provides early embryos with a robust mechanism to enforce the Hertwig rule.

Our quantifications also show that the CCs in the two blastomeres remain coplanar to each other while they rotate to achieve the final alignment. We find that the tilt angle between the CCs and the mother spindle converges to 15° (and not 0°), similar to the tilt angle found in another ascidian species at the 4- to 8-cell stage cell division (Godard et al., 2021; Negishi et al., 2007). Ectopically inducing more cortical pulling increased the tilt angle difference between the two CCs and prevented 4-cell stage embryos from being planar. Moreover, the persistence of coplanar, but not square, divisions in CMF seawater-treated embryos further implies that cortical inputs primarily refine coplanarity, while ER-based cytoplasmic forces provide the dominant contribution to CC rotation and global spindle alignment.

Our findings expand the repertoire of known mechanisms by which cells can achieve precise spatial organization during development and highlight the evolutionary diversity of strategies employed by different organisms. Proper spindle orientation is not only critical for ensuring correct cleavage patterns and cell fate specification but also for the establishment of tissue architecture and organogenesis. The mechanisms uncovered in ascidian embryos may thus inform our understanding of how similar processes are regulated in other organisms, and may provide insights into the evolution of developmental strategies across metazoans.

402 **MAIN FIGURES**

403

404 **Figure 1**

405

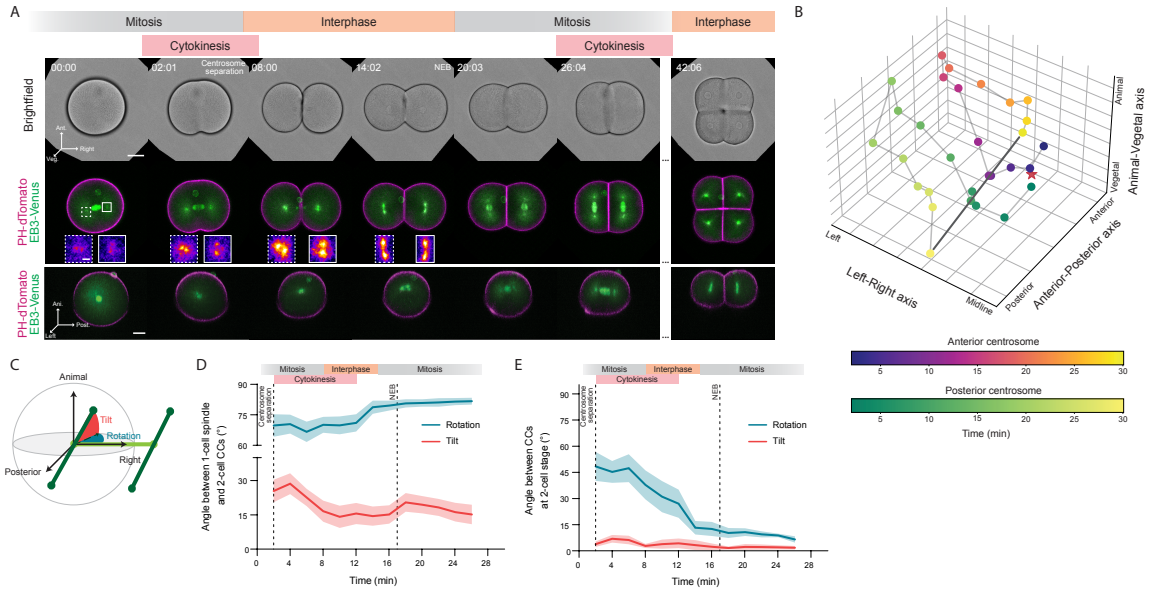

406

407

408 **Figure 1: CCs become parallel and coplanar during interphase of the 2-cell stage.**

409 **(A)** Brightfield, confocal fluorescent images of a central z-slice of the plasma membrane (magenta),
410 and maximum intensity projections of centrosomes (green) in an ascidian embryo from 1-cell stage
411 metaphase (time = 00:00) to 4-cell stage interphase (time = 42:06). Top and middle rows show the
412 vegetal view, and bottom row shows the side view. Insets are magnifications of the left (dashed square)
413 and right (solid square) CC. Ant. is anterior, Veg. is vegetal, Ani. is animal, Post. is posterior, NEB is
414 nuclear envelope breakdown. Time is in minutes:seconds. Scale bar, 30 µm. Inset scale bar, 5 µm.

415 **(B)** 3D plot of the relative positions over time of the anterior and posterior centrosomes of the CC in
416 the left cell of a 2-cell stage ascidian embryo. Time is coded in the respective color bar. The star
417 represents the position of the left pole of the mitotic spindle at 1-cell stage, and the grey line
418 represents the final orientation of the 2-cell stage spindle.

419 **(C)** Graphical representation of the tilt and rotation angles in spherical coordinates between the CCs
420 or the spindles at the 2-cell stage (dark green) and the spindle at the 1-cell stage (light green).

421 **(D)** Plot of the rotation (blue) and tilt (red) angles between the 2-cell stage CCs or spindles and the 1-
422 cell stage spindle as a function of time. The dashed line at 17 min indicates NEB. *N* = 9 embryos, *n* = 18
423 cells. Error bars, standard error of the mean.

424 **(E)** Plot of the rotation (blue) and tilt (red) angles between the left and right CCs or spindles at 2-cell
425 stage as a function of time. The dashed line at 17 min indicates NEB. *N* = 9 embryos. Error bars,
426 standard error of the mean.

427

428

429

430

431

432

Figure 2

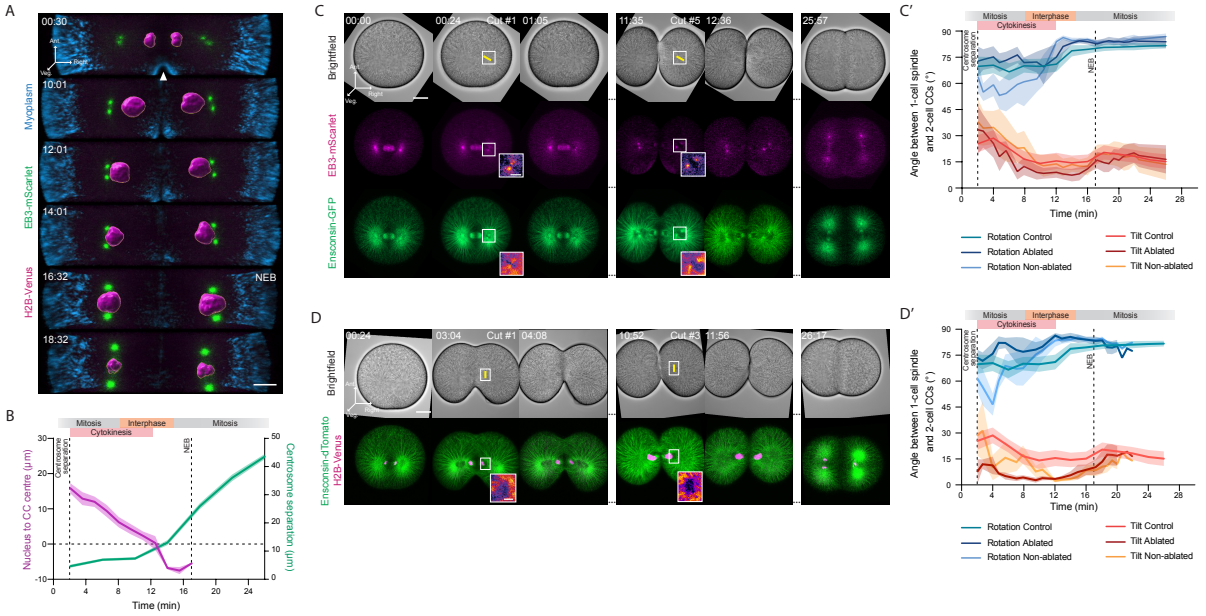

Figure 2: Migration of the CC and nucleus during interphase of the 2-cell stage.

(A) Confocal maximum intensity projections of the centrosomes (green), mitochondria (cyan), and segmented nuclei (magenta) in an ascidian embryo during interphase of the 2-cell stage. Ant. is anterior, Veg. is vegetal, and NEB is nuclear envelope breakdown. Arrowhead marks the cytokinetic furrow. Time is in minutes:seconds. Scale bar, 10 µm

(B) Plot of the distance between the edge of the nucleus and the center of the CC (magenta, left *y*-axis; *N* = 6 embryos, *n* = 12 cells) and centrosome separation within a CC (green, right *y-axis*; *N* = 9 embryos, *n* = 18 cells) as a function of time. The dashed line at 17 min indicates NEB. Error bars, standard error of the mean.

(C) Brightfield and confocal maximum intensity projections of centrosomes (magenta, middle row) and microtubules (green, bottom row) during laser ablation of microtubules between the centrosomes. The yellow line demarcates the ablation site. Ant. is anterior, Veg. is vegetal. Time is in minutes:seconds. Scale bar, 30 µm. Inset scale bar, 5 µm.

(C') Plot of the rotation and tilt angles between the 2-cell stage CCs or spindles and the 1-cell stage spindle as a function of time in control embryos (*N* = 9 embryos, *n* = 18 cells), ablated cell (*N* = 5 embryos, *n* = 5 cells), and non-ablated cell (*N* = 5 embryos, *n* = 5 cells) of laser-ablated embryos between the centrosomes. The dashed line at 17 min indicates NEB. Error bars, standard error of the mean.

(D) Brightfield and confocal maximum intensity projections of the DNA (magenta) and microtubules (green) during laser ablation of microtubules between the nucleus and the CC. The yellow line demarcates the ablation site. Ant. is anterior, Veg. is vegetal. Time is in minutes:seconds. Scale bar, 30 µm. Inset scale bar, 5 µm.

(D') Plot of the rotation and tilt angles between the 2-cell stage CCs or spindles and the 1-cell stage spindle as a function of time in control embryos (*N* = 9 embryos, *n* = 18 cells), ablated cell (*N* = 4 embryos, *n* = 4 cells), and non-ablated cell (*N* = 4 embryos, *n* = 4 cells) of laser-ablated embryos between the centrosomes and the nucleus. The dashed line at 17 min indicates NEB. Error bars, standard error of the mean.

Figure 3

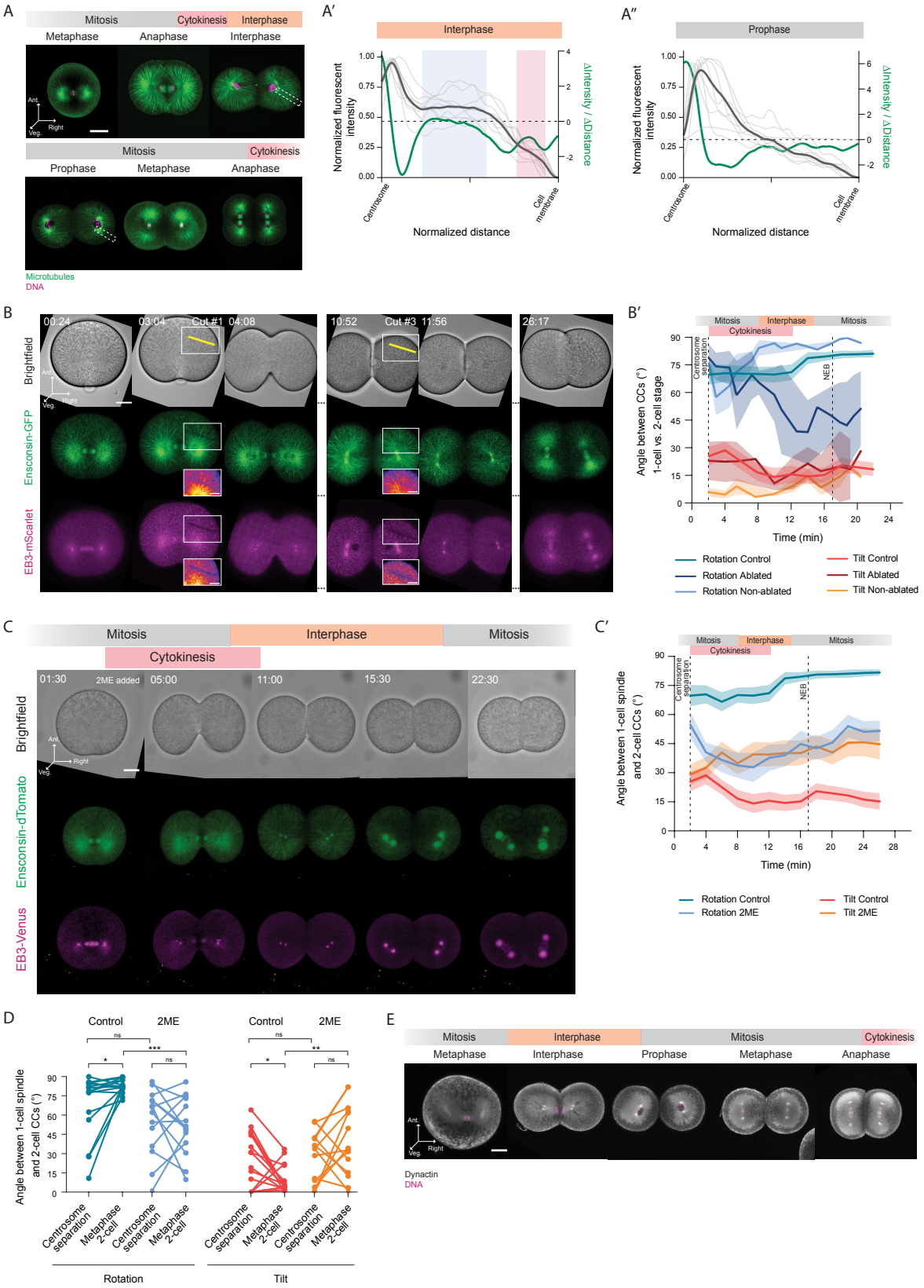
A
Mitosis
Cytokinesis
Interphase
Metaphase
Anaphase
Interphase
Ant.
Right
Veg.
Mitosis
Cytokinesis
Prophase
Metaphase
Anaphase
Microtubules
DNA
A′
Interphase
Normalized fluorescent intensity
ΔIntensity / ΔDistance
Centrosome
Cell membrane
Normalized distance
A″
Prophase
Normalized fluorescent intensity
ΔIntensity / ΔDistance
Centrosome
Cell membrane
Normalized distance
B
Brightfield
Ensconsin-GFP
EB3-mScarlet
00:24
03:04
Cut #1
04:08
10:52
Cut #3
11:56
26:17
B′
Mitosis
Interphase
Mitosis
Cytokinesis
Centrosome separation
NEB
Angle between CCs (°) 1-cell vs. 2-cell stage
Time (min)
Rotation Control
Rotation Ablated
Rotation Non-ablated
Tilt Control
Tilt Ablated
Tilt Non-ablated
C
Mitosis
Interphase
Mitosis
Cytokinesis
01:30
2ME added
05:00
11:00
15:30
22:30
Brightfield
Ensconsin-dTomato
EB3-Venus
C′
Mitosis
Interphase
Mitosis
Cytokinesis
Centrosome segregation
NEB
Angle between 1-cell spindle and 2-cell CCs (°)
Time (min)
Rotation Control
Rotation 2ME
Tilt Control
Tilt 2ME
D
Control
2ME
Control
2ME
ns
***
*
ns
ns
**
*
ns
Angle between 1-cell spindle and 2-cell CCs (°)
Centrosome separation
Metaphase 2-cell
Centrosome separation
Metaphase 2-cell
Centrosome separation
Metaphase 2-cell
Centrosome separation
Metaphase 2-cell
Rotation
Tilt
E
Mitosis
Interphase
Mitosis
Cytokinesis
Metaphase
Interphase
Prophase
Metaphase
Anaphase
Ant.
Right
Veg.
Dynactin
DNA

Figure 3: Forces along astral microtubules are essential for the orientation of CCs.

(A) Confocal fluorescent images of a central z-slice of ascidian embryos from 1-cell stage metaphase to 2-cell stage anaphase stained for microtubules (green) and DNA (magenta). Ant. is anterior, Veg. is vegetal. The dashed area indicates the area analyzed in A' and A''. Scale bar, 40 µm.

(A', **A'')** Fluorescent intensity profiles show the distribution of microtubules from the centrosome to the cell membrane in embryos in interphase (left *y* axis; *N* = 9 embryos) and in prophase (left *y* axis; *N* = 8 embryos). The green line (right *y* axis) represents the change in the average intensity profile over the distance.

(B) Brightfield and confocal maximum intensity projections of microtubules (green, middle row) and centrosomes (magenta, bottom row) during laser ablation of astral microtubules. The yellow line demarcates the ablation site. Ant. is anterior, Veg. is vegetal. Time is in minutes:seconds. Scale bar, 30 µm. Inset scale bar, 20 µm.

(B') Plot of the rotation and tilt angles between the 2-cell stage CCs or spindles and the 1-cell stage spindle as a function of time in control embryos (*N* = 9 embryos, *n* = 18 cells), ablated cell (*N* = 4 embryos, *n* = 4 cells), and non-ablated cell (*N* = 4 embryos, *n* = 4 cells) of laser-ablated embryos. The dashed line at 17 min indicates NEB. Error bars, standard error of the mean.

(C) Brightfield and confocal maximum intensity projections of microtubules (green, middle row) and centrosomes (magenta, bottom row) in 2ME-treated embryos. Ant. is anterior, Veg. is vegetal. Time is in minutes:seconds. Scale bar, 30 µm.

(C') Plot of the rotation and tilt angles between the 2-cell stage CCs or spindles and the 1-cell stage spindle as a function of time in control embryos (*N* = 9 embryos, *n* = 18 cells) and 2ME-treated embryos (*N* = 7 embryos, *n* = 14 cells). The dashed line at 17 min indicates NEB. Error bars, standard error of the mean.

(C'') Plot of the initial (Centrosome separation) and final (Metaphase 2-cell) rotation (left) and tilt (right) angles between the 2-cell stage CCs or spindles at 2-cell stage with respect to the 1-cell stage spindle in control embryos (*N* = 9 embryos, *n* = 18 cells; rotation: paired Wilcoxon test, *P=0.0131; tilt: paired Wilcoxon test, *P=0.0250) and 2ME-treated embryos (*N* = 7 embryos, *n* = 14 cells; rotation and tilt: paired t test, ns). Control vs. 2ME rotation angle: Kruskal-Wallis test (***P=0.0001) with Dunn's multiple comparisons test (ns, ***P=0.0001). Control vs. 2ME tilt angle: Kruskal-Wallis test (*P=0.0101) with Dunn's multiple comparisons test (ns, **P<0.0025). ns, not significant.

(D) Confocal fluorescent images of a central z-slice of ascidian embryos from 1-cell stage metaphase to 2-cell stage anaphase stained for dynactin (grey) and DNA (magenta). Ant. is anterior, Veg. is vegetal. Scale bar, 30 µm.

Figure 4

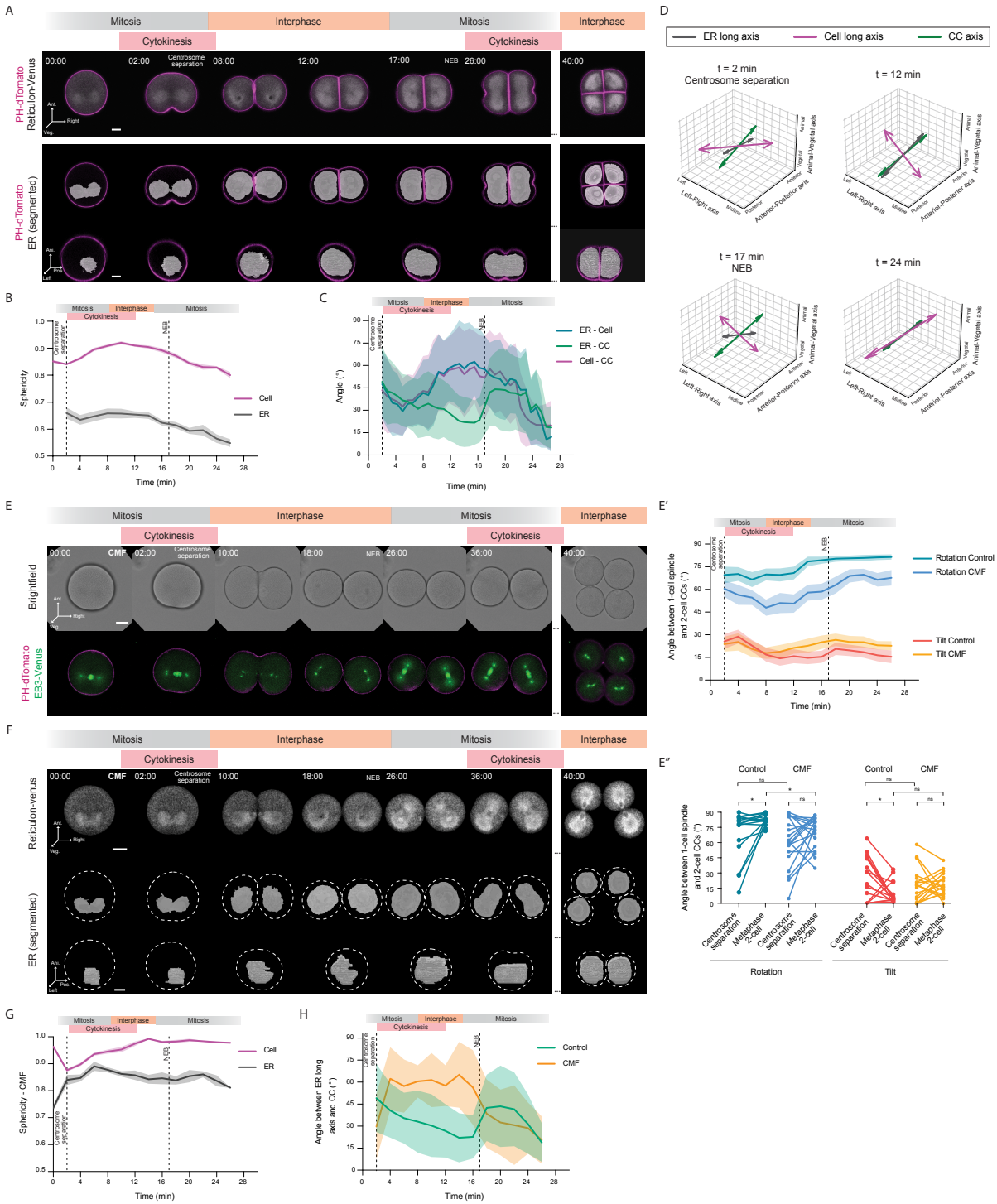

Figure 4: Cytoplasmic pulling controls rotation of the CCs.

(A) Confocal fluorescent images of a central z-slice of the plasma membrane (magenta) and the endoplasmic reticulum (grey) in an ascidian embryo from 1-cell stage metaphase to 4-cell stage interphase. Middle and bottom rows show a top and side view, respectively, of the membrane (magenta) and the segmented ER (grey). Ant. is anterior, Veg. is vegetal, Ani. is animal, Post. is posterior, and NEB is nuclear envelope breakdown. Time is in minutes:seconds. Scale bar, 30 µm.

(B) Plot of the sphericity of the cell (magenta; *N* = 14 embryos) and the ER (grey; *N* = 12 embryos) as a function of time in control embryos. The dashed line at 17 min indicates NEB. Error bars, standard error of the mean.

(C) Plot of the angle between the long axes of the ER and the cell (blue), the ER and the CCs (green), and the cell and the CCs (red) as a function of time in control embryos. The dashed line at 17 min indicates NEB. Error bars, standard deviation (s.d.). Mean and s.d. were estimated by bootstrap method (5000 iterations).

(D) 3D plots of the average long axes of the cell (magenta), the ER (grey), and the CCs (green) at 2, 12, 17, and 24 minutes of the left cells of ascidian embryos after metaphase of the 1-cell stage. NEB is nuclear envelope breakdown. For visualization purposes, the length of the long axes of the cell and the CCs is doubled.

(E) Brightfield, confocal fluorescent images of a central z-slice of the plasma membrane (magenta), and maximum intensity projections of centrosomes (green) in an ascidian embryo in CMF seawater from 1-cell stage metaphase to 4-cell stage interphase. Ant. is anterior, Veg. is vegetal, Ani. is animal, Post. is posterior, and NEB is nuclear envelope breakdown. Time is in minutes:seconds. Scale bar, 40 µm.

(E') Plot of the rotation and tilt angles between the 2-cell stage CCs or spindles and the 1-cell stage spindle as a function of time in control embryos (*N* = 9 embryos, *n* = 18 cells) and CMF-treated embryos (*N* = 10 embryos, *n* = 20 cells). The dashed line at 17 min indicates NEB. Error bars, standard error of the mean.

(E'') Plot of the initial (Centrosome separation) and final (Metaphase 2-cell) rotation (left) and tilt (right) angles between the 2-cell stage CCs or spindles and the 1-cell stage spindle in control embryos (*N* = 9 embryos, *n* = 18 cells; rotation: paired Wilcoxon test, *P=0.0131; tilt: paired Wilcoxon test, *P=0.0250) and CMF-treated embryos (*N* = 10 embryos, *n* = 20 cells; rotation and tilt: paired t test, ns). Control vs. CMF rotation angle: Kruskal-Wallis test (*P=0.0194) with Dunn's multiple comparisons test (ns, *P=0.0276). Control vs. CMF tilt angle: Kruskal-Wallis test (ns) with Dunn's multiple comparisons test (ns). ns, not significant.

(F) Confocal fluorescent images of the endoplasmic reticulum (top row) and its segmentation (middle row is the top view and bottom row is the side view) in an ascidian embryo from 1-cell stage metaphase to 4-cell stage interphase in CMF seawater. Ant. is anterior, Veg. is vegetal, Ani. is animal, Post. is posterior, and NEB is nuclear envelope breakdown. Time is in minutes:seconds. Scale bar, 30 µm.

(G) Plot of the sphericity of the cell (magenta; *N* = 4 embryos) and the ER (grey; *N* = 10 embryos) as a function of time in CMF-treated embryos. The dashed line at 17 min indicates NEB. Error bars, standard error of the mean.

(H) Plot of the angle between the long axis of the ER and the CCs or spindles as a function of time in control embryos (green, taken from C) and in CMF-treated embryos (orange). The dashed line at 17 min indicates NEB. Error bars, standard deviation.

Figure 5

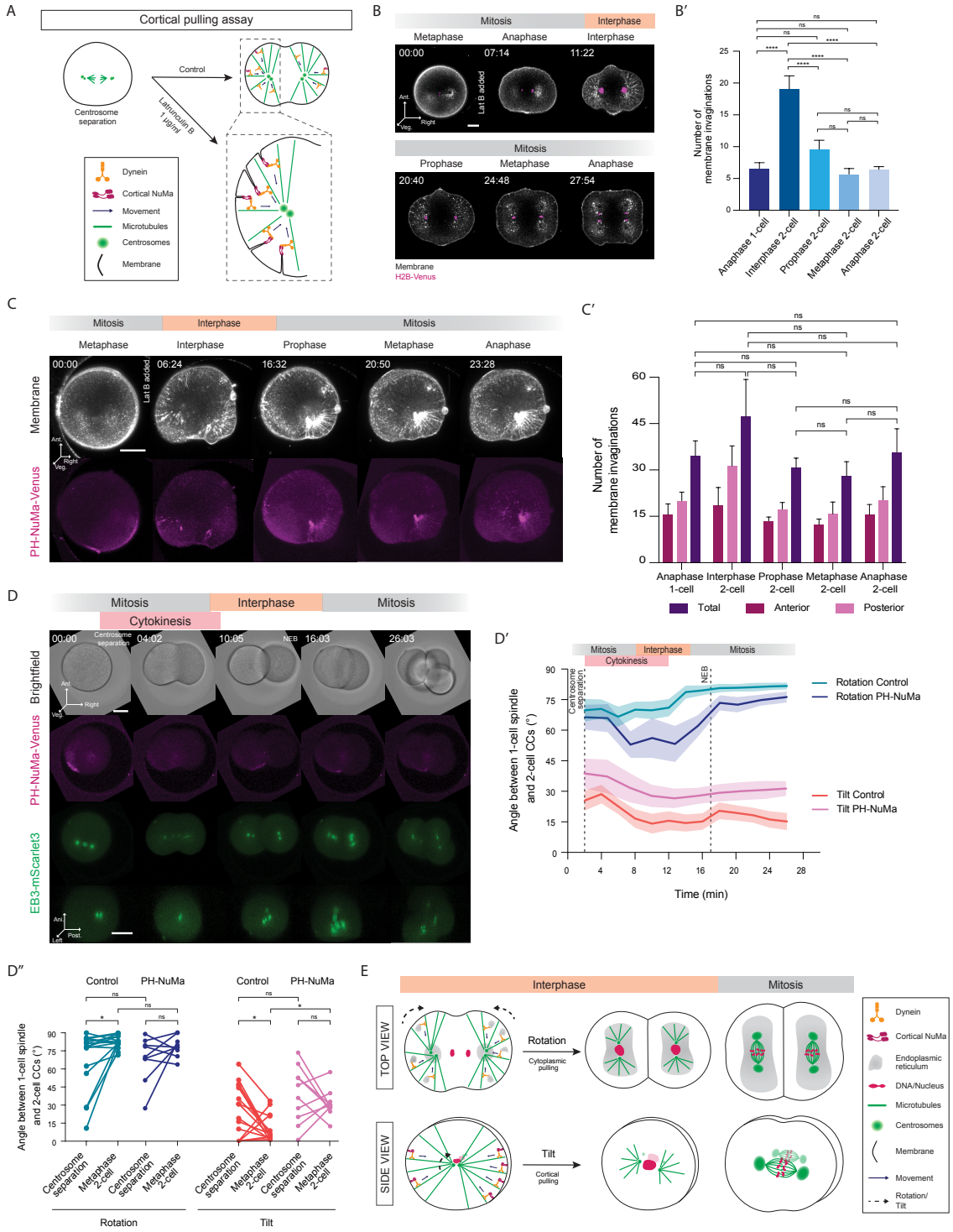

Figure 5: Tilt along the anterior-posterior axis is controlled by cortical pulling forces.

(A) Schematic representation of the cortical pulling assay.

(B) Confocal maximum intensity projections over 6 central z-slices of the plasma membrane (grey) and DNA (magenta) in an ascidian embryo from 1-cell stage metaphase to 2-cell stage anaphase, treated with 1µg/ml Latrunculin B from 1-cell stage anaphase. Ant. is anterior, Veg. is vegetal. Time is in minutes:seconds. Scale bar, 30 µm.

578 **(B')** Bar plot of the average number of membrane invaginations as a function of the cell cycle stage. (*N*
579 = 13 embryos). One-way ANOVA (****P<0.0001) and Tukey's multiple comparisons tests
580 (****P<0.0001; ns - not significant). Error bars, standard error of the mean.
581 **(C)** Confocal maximum intensity projections over 6 central z-slices of PH-NuMA (magenta) and
582 membrane (grey) in an ascidian embryo expressing PH-NuMA and treated with 1µg/ml Latrunculin B
583 from 1-cell stage anaphase. Scale bar, 40µm.
584 **(C')** Bar plot of the average number of membrane invaginations (anterior, posterior, and total) as a
585 function of the cell cycle stage in embryos expressing PH-NuMA and treated with 1µg/ml Latrunculin
586 B. (*N* = 4 embryos). Kruskal-Wallis test and Dunn's multiple comparisons test. Error bars, standard error
587 of the mean. ns, not significant.
588 **(D)** Brightfield and confocal maximum intensity projections of PH-NuMA (magenta) and centrosomes
589 (green) in embryos expressing PH-NuMA. Ant. is anterior, Veg. is vegetal, Ani. is animal, Post. Is
590 posterior. Time is in minutes:seconds. Scale bar, 40 µm.
591 **(D')** Plot of the rotation and tilt angles between the 2-cell stage CCs or spindles and the 1-cell stage
592 spindle as a function of time in control embryos (*N* = 9 embryos, *n* = 18 cells) and embryos expressing
593 PH-NuMA (*N* = 5 embryos, *n* = 10 cells). The dashed line at 17 min indicates NEB. Error bars, standard
594 error of the mean.
595 **(D'')** Plot of the initial (Centrosome separation) and final (Metaphase 2-cell) rotation (left) and tilt
596 (right) angles between the 2-cell stage CCs or spindles and the 1-cell stage spindle in control embryos
597 (*N* = 9 embryos, *n* = 18 cells; rotation: paired Wilcoxon test, *P=0.0131; tilt: paired Wilcoxon test,
598 *P=0.0250) and embryos expressing PH-NuMA (*N* = 7 embryos, *n* = 14 cells; rotation and tilt: paired t
599 test, ns). Control vs. PH-NuMA rotation angle: Kruskal-Wallis (*P=0.0201) with Dunn's multiple
600 comparisons test (ns). Control vs. PH-NuMA tilt angle: Kruskal-Wallis (**P=0.0073) with Dunn's
601 multiple comparisons test (ns, *P=0.0169). ns, not significant.
602 **(E)** Model of the mechanisms controlling CC positioning during the 2-cell stage: cytoplasmic dynein-
603 dependent pulling along astral microtubules controls the 90° rotation of the CCs with respect to the 1-
604 cell stage spindle. Dynein motors on the ER surface move towards the CCs, thus forming the
605 pericentromeric ER domains. These domains act as a proxy for cell shape, dictating the rotation of the
606 CCs during interphase to generate parallel spindles at the 2-cell stage. Concomitantly, cortical dynein
607 generates cortical pulling forces at the end of astral microtubules that control the tilt of the CCs,
608 ensuring the coplanarity of sister CCs and the planar geometry of the 4-cell stage ascidian embryo.
609
610
611
612
613
614
615
616
617
618
619
620
621
622

623 **MATERIALS AND METHODS**

624 **Animal Collection and Maintenance and Embryo Handling**

625 Adult *Phallusia mammillata* were collected in Sète (France) and kept at 16 °C in the aquaria of the
626 Centre de Resources Biologiques (CRB) of the Institut de la Mer de Villefranche (IMEV), which is an
627 EMBRC-France certified service (https://www.embrc-france.fr/fr/nos-services/fourniture-de-
628 ressources-biologiques/organismes-modeles/ascidie-phallusia-mammillata). All experiments were
629 performed at 18-19 °C. Oocytes and sperm were obtained after animal dissection and used on the day
630 of collection. Oocytes were chemically dechorionated in a 0.1 % trypsin solution (Merck, T8003) in
631 micro-filtered natural sea water (MFSW; Nalgene 0.2 µm filters, cat. no. Z370584) for 90 min under
632 gentle stirring and kept in MFSW until fertilization with 6 µl sperm that was activated by resuspension
633 in 1 ml of MFSW at pH 9.2.
634 Embryos were cultured either in MFSW or in Ca^{2+} and Mg^{2+}-free (CMF) seawater supplemented with 1
635 mM EDTA (Sardet et al., 2011).
636

637 **Cloning of Expression Constructs**

638 To generate the pSPE3-EB3-mScarlet plasmid, the EB3 coding sequence was amplified from pRN3-EB3-
639 3xVenus vector using the following primers with EcoRI and XhoI sites, respectively: 5'-
640 GAATTCAAAATGGCCGTCAATGTGTACTCCACAT-3' and 5'-CTCGAGGTACTCGTCCTGGTCTTCTTGTTGA-3'.
641 The mScarlet coding sequence (including stop codon) was amplified from the plasmid pSPE3-iMyo-
642 mScarlet (Caballero-Mancebo et al., 2024) using the following primers with XhoI and NotI sites,
643 respectively: 5'-CTCGAGATGGTGAGCAAGGGCGAGGCAGTG-3' and 5'-
644 GCGGCCGCCTACTTGTACAGCTCGTCCATGCC-3'. To generate the pSPE3-EB3-mScarlet plasmid, the PCR
645 products were ligated into a pSPE3-Rfa destination vector (Roure et al., 2007) that had been previously
646 digested with EcoRI and NotI.
647 To generate the pSPE3-Reticulon-Venus plasmid, the *Phallusia mammillata* reticulon coding sequence
648 (GenBank CAB3265822.1) was amplified from a cDNA library using the following primers: 5'-
649 CACCATGGAGTATGAAACGAGCCC-3' and 5'-CTCTGCTTTAGGCTTGGCACC-3'. The PCR product was used
650 to generate an entry vector using the pDONR/TOPO (p3M-Reticulon). The entry vector was
651 recombined with the destination vector pSPE3-Rfa-Venus (Roure et al., 2007).
652 To generate the pSPE3-PH-NuMA-Venus plasmid, the *Phallusia mammillata* NuMA coding sequence
653 (GenBank CAB3265828.1) was amplified from a cDNA library using hybridizing primers: 5'-
654 GAGCTCAACATCATGGATGATGACGAAA-3' and 5'-GTCTGAATCCAAAAAAGAAGGGTGGGCG-3'. The PH
655 coding sequence was amplified from pSPE3-PH-dTomato plasmid (Prodon et al., 2010) using the
656 following hybridizing primers: 5'-AAGCAGGCTCCGCGGCCGCCCCCTTCA-3' and 5'-
657 GAGCTCAACATCATGGATGATGACGAAA-3'. After hybridization, the full PH-NuMA coding sequence was
658 amplified using the following primers: 5'-ACAAGTTTGTACAAAAAAGCAGGCTCCGCGGCCGCCCCCTTCA-
659 3' and 5'-GTCTGAATCCAAAAAAGAAGGGTGGGCGCGCCGACCCAGCTTTCTTGTACAAAGTGGT-3'. The
660 final PCR product was used to generate an entry vector using the pDONR/TOPO (p3M-PH-NuMA). The
661 entry vector was recombined with the destination vector pSPE3-Rfa-Venus (Roure et al., 2007).
662

663 **mRNA Microinjections**

664 Microinjections were performed as described(McDougall et al., 2014). Microinjection needles (Harvard
665 Apparatus, 30-0035) were pulled with a PN-30 puller (Narishige) and mounted on a micromanipulation
666 setup (MMO-203, Narishige) attached to an Olympus IX70 microscope. Dechorionated unfertilized
667 eggs were placed into a glass wedge mounted onto a 400 µl Perspex mounting chamber (McDougall

668 et al., 2014). *In vitro* mRNA synthesis was performed using the mMESSAGE mMACHINE T3
669 Transcription Kit (Ambion, AM1343). The following mRNAs were injected: EB3-3xVenus (Rosfelter et
670 al., 2024), EB3-mScarlet (this study), Ensconsin-3xGFP (Costache et al., 2017), Ensconsin-dTomato
671 (Costache et al., 2017), H2B-Venus (Prodon et al., 2010), PH-dTomato (Prodon et al., 2010), PH-NuMA-
672 Venus (this study), and Reticulon-Venus (this study). mRNAs were injected at a concentration of 2-4
673 µg/µl using a high-pressure system (Narishige IM300) and incubated at 16 °C overnight before the
674 experiment.
675
676 **Myoplasm and Plasma Membrane Labeling**
677 Dechorionated unfertilized oocytes or zygotes were incubated in a 1 µM solution of MitoTracker™
678 Deep Red FM (Thermo Fisher, M22426) to label the myoplasm and/or in a 1 µM solution of CellMask™
679 Orange (Thermo Fisher, C10045) in MFSW for 5 min and washed in MFSW before imaging.
680
681 **Cytoskeletal Inhibitors**
682 To soften the cortex, 1 µg/ml Latrunculin B (Merck, L5288) was added to the imaging dish 40 minutes
683 post fertilization (right before first cell division) and left in the medium for the remainder of the
684 experiment.
685 To interfere with dynamic microtubules, 1 µg/ml 2-methoxyestradiol (Merck, M6383) was added to
686 the imaging dish 40 minutes post fertilization (right before first cell division) and left in the medium for
687 the remainder of the experiment.
688
689 **Confocal Live Imaging**
690 Embryos were mounted 30 minutes post fertilization in glass-bottom dishes (Cellvis, D35-10-0-N)
691 coated with 1% low gelling temperature agarose (Merck, A2576) in MFSW. Embryos were imaged in
692 either an inverted Leica TCS SP8 confocal microscope or an inverted Leica Stellaris confocal microscope
693 using a HCPL APO CS2 40x/1.1 NA water immersion objective (Leica) and Hybrid detectors. Embryos
694 were imaged *in toto* with an optical section thickness of 3 µm every 120-180 s. For membrane
695 invagination experiments, the frame rate was reduced to 30 s, and for fixed samples, the optical
696 section was 1 µm.
697
698 **Laser Ablation**
699 Embryos were mounted 30 minutes post fertilization as for confocal live imaging and imaged on a Zeiss
700 LSM980 confocal microscope equipped with a two-photon pulsed laser using a C-Aprochromat 40x/1.1
701 NA water immersion objective. Microtubules between centrosomes or between centrosomes and the
702 nucleus were cut along a 10 µm line and astral microtubules were cut along 50 µm lines in 3 z planes,
703 all of which were performed with a two-photon Coheren Axon 920-2 laser (2.5W). For ablation, the
704 two-photon laser was used at full power, and the power received at the focal point is estimated at 2.8
705 $\cdot 10^{12}$ W/m^2. Embryos were imaged over 50 central z-slices with an optical section thickness of 1 µm
706 every 13 s.
707
708 **Antibody Production**
709 The ascidian-specific anti-dynactin mouse polyclonal antibody was produced by fusing 1002 base pairs,
710 amino acids 35 to 334, of the *Ciona intestinalis* dynactin subunit 1 protein (GenBank AP042712.1) to a
711 6-His tag at the C terminus and cloned into the vector pET11. Expression in bacteria was induced with
712 IPTG, and the dynactin fusion protein was purified on a nickel column and eluted with imidazole

713 according to the manufacturer's instructions (Potrino Ni-NTA column, Macherey-Nagel). Immunization
714 of mice was performed by Covalab (France), and sera was obtained after 57 days were used directly
715 without further purification.
716
717 **Western Blot**
718 Anti-dynactin antibody's specificity was validated by Western blot analysis showing a single band at
719 ~55 kDa corresponding to dynactin (Fig. S3C).
720 2 and 8-cell stage embryos were collected in a small volume of MFSW and mixed with the same volume
721 of 2x Laemmli sample buffer (100 mM Tris-HCL pH 6.8, 4% SDS, 0.2% Bromophenol Blue, 20% glycerol
722 and 200 mM dithiothreitol). Samples were heated for 5 min at 95 °C and then stored at -20 °C. Proteins
723 were separated by electrophoresis on SDS-polyacrylamide gels and transferred to a nitrocellulose
724 membrane. Membranes were stained briefly with Ponceau-S, then washed with TBS-Tw (20 mM Tris
725 Base and 150 mM NaCl plus 0.1% Tween-20), and blocked for at least 1 hour in TBS-Tw containing 5%
726 dry milk powder. Immunoblots were then incubated in anti-dynactin primary antibody diluted 1:1000
727 overnight at 4 °C. Membranes were then washed three times with TBS-Tw and incubated with an anti-
728 mouse horseradish peroxidase-conjugated secondary antibody (Jackson ImmunoResearch, 115-035-
729 003) at 1:10,000 dilution in TBS-Tw + 5% dry milk powder for 2 hours at room temperature. After three
730 washes in TBS-Tw, signal detection was carried out using the SuperSignal™ West PLUS Pico
731 chemiluminescent substrate (ThermoFisher Scientific, 34580), and images were acquired with a Fusion
732 FX system (Vilber Lourmat, Collegien, France).
733
734 **Immunostaining**
735 Embryos were fixed in 100% methanol (VWR Chemicals, 67-56-1), which had been pre-chilled at −20°C,
736 and then stored at -20°C. Samples were rehydrated by three washes in PBS containing 0.1% Tween
737 (PBS-Tw), then blocked in PBS-Tw containing 1% BSA for 1 hour at room temperature. Primary
738 antibodies to tyrosinated alpha tubulin (rat anti-alpha-tubulin tyrosinated, monoclonal YL1/2, Merck,
739 MAB1864-I) or to dynactin subunit 1 (mouse polyclonal, custom made, see above) were added at a
740 dilution of 1/500 in blocking buffer and incubated for at least 24 hours at 4 °C. After incubation,
741 samples were washed three times in PBS-Tw, and fluorescent anti-rat (Jackson ImmunoResearch, 112-
742 095-003) or anti-mouse secondary antibodies (Jackson ImmunoResearch, 115-175-146) were added at
743 a dilution of 1/200. After further incubation at room temperature for 1-2 hours, samples were washed
744 in PBS-Tw, labelled with Hoechst 33342 (final concentration 5 µg/ml, Merck, TA9H97BAECD2) for 10
745 minutes, washed twice more in PBS-Tw, and mounted on glass slides in CitiFluor AF1 (Electron
746 Microscopy Services, 17970-25). To prevent embryo compression or breakage, coverslips were
747 elevated by application of small spacers of modelling clay at the corners.
748
749 **3D Tracking of Centrosomes and Angle Quantification**
750 Confocal fluorescent z-stacks of embryos injected with EB3-3xVenus and PH-dTomato were stabilized
751 using the MultiStackReg (Thevenaz et al., 1998) plugin in Fiji (Schindelin et al., 2012). Centrosomes
752 were then tracked using the MTrackJ (Meijering et al., 2012) plugin in Fiji, and their 3D coordinates
753 (Ci_x, Ci_y, Ci_z) were used to calculate the polar angles (rotation and tilt) with the y-axis (embryonic
754 anterior-posterior axis) as reference.
755
756
757

Centrosome separation

The 3D coordinates of each centrosome were used to calculate the distance between each centrosome within a CC: $d = \sqrt{(C1_x - C2_x)^2 + \left(C1_y - C2_y\right)^2 + (C1_z - C2_z)^2}$

Distance Between the Nucleus and the CC

Confocal fluorescent z-stacks of embryos injected with H2B-Venus and EB3-mScarlet were stabilized using MultiStackReg plugin in Fiji. Centrosomes were then tracked using the MTrackJ plugin in Fiji, and their 3D coordinates (Ci_x, Ci_y, Ci_z) used to calculate the midpoint of the CC, $M_{CC} = \left(\frac{C1_x+C2_x}{2}, \frac{C1_y+C2_y}{2}, \frac{C1_z+C2_z}{2}\right)$. The nucleus of each cell was segmented and tracked using the Surface tool in Imaris (Bitplane). Then the distance at every time point between the nucleus (N_x, N_y, N_z) and the CC midpoint was calculated: $d = \sqrt{(M_x - N_x)^2 + \left(M_y - N_y\right)^2 + (M_z - N_z)^2}$. The radius of the nucleus was subtracted from the distance to reflect the time when the edge of the nucleus reaches the center of the CC.

Microtubule Intensity Profile

The intensity profiles of microtubules were made using the line tool of 15-pixel thickness in Fiji from the centrosome to the plasma membrane. The intensity values shown were normalized to the maximum intensity value along each line. The distance between the centrosome and the plasma membrane was also normalized.

Membrane Invagination Quantification

Confocal fluorescent z-stacks of embryos incubated in CellMask™ Orange to label the plasma membrane were stabilized using MultiStackReg plugin in Fiji. 10 confocal z-slices over the equator of the embryo were sum projected. The number of membrane invaginations was counted manually by counting the invaginations present at 2-10 µm from the plasma membrane (Rosfelter et al., 2024) at the times indicated in Fig. 5B and C.

Endoplasmic Reticulum Segmentation

Confocal fluorescent z-stacks of embryos injected with either Reticulon-Venus and PH-dTomato, Reticulon-Venus and Ensconsin-dTomato or Reticulon-Venus and EB3-mScarlet were stabilized using the MultiStackReg plugin in Fiji. For segmentation a Gaussian filter (sigma = 2) was applied and segmented using Ilastik software (Berg et al., 2019) and the pixel classification method. Segmentations were then manually corrected using Napari (Chiu et al., 2022).

Plasma Membrane Segmentation

Confocal fluorescent z-stacks of embryos injected with PH-dTomato were stabilized using the MultiStackReg plugin in Fiji and segmented using Cellpose (Stringer et al., 2021). Segmentations were then manually corrected using Napari.

Shape Analysis

Principal component analysis (PCA) of segmented membrane and ER timelapses was performed in order to obtain the direction of the 3 main axes using a custom-made Python script. To compute the

length of the main axes (a, b, c), each voxel from the segmented images was projected onto each axis, and sphericity was calculated as: $sphericity = \sqrt[3]{c^2/ab}$.

Statistical analysis

Statistical analysis was performed using Prism 8 (GraphPad). The statistical test used and the resulting P values are indicated in each figure legend. *N* was considered an independent experiment, and *n* denotes the number of cells; *N* and *n* are indicated in each figure. No statistical method was used to predetermine sample size. The experiments were not randomized.

ACKNOWLEDGEMENTS

We would like to thank Hervé Turlier for fruitful discussions and the Microscopy Imaging Platform (PIM) and the animal facility (CRB) of the Institut de la Mer de Villefranche (IMEV), supported by EMBRC-France, whose French state funds are managed by the ANR within the Investments of the Future program under reference ANR-10-INBS-0. This project was funded by the Agence Nationale de la Recherche (France) grant "InvBlastula" (ANR-22-CE13-0036-01).

AUTHORS CONTRIBUTIONS

S.C.-M., A.M., and R.D. designed the research. S.C.-M. performed the experiments and analyzed the experimental data. D.G.S. contributed to the data analysis. J.C. performed the immunostainings and antibody validations. S.C.-M. and S.B-A. performed the laser ablation experiments. L.B. created the pSPE3-EB3-mScarlet, pSPE3-Reticulon-Venus, and pSPE3-PH-NuMA-Venus constructs. S.C.-M. and R.D. wrote the manuscript.

DECLARATION OF INTERESTS

The authors declare no competing interests.

REFERENCES

Anjur-Dietrich, M.I., Hererra, V.G., Farhadifar, R., Wu, H., Merta, H., Bahmanyar, S., Shelley, M.J., Needleman, D.J., 2024. Mechanics of spindle orientation in human mitotic cells is determined by pulling forces on astral microtubules and clustering of cortical dynein. Dev. Cell.

Berends, C.W.H., Muñoz, J., Portegijs, V., Schmidt, R., Grigoriev, I., Boxem, M., Akhmanova, A., Heck, A.J.R., van den Heuvel, S., 2013. F-actin asymmetry and the endoplasmic reticulum–associated TCC-1 protein contribute to stereotypic spindle movements in the Caenorhabditis elegans embryo. Mol. Biol. Cell 24, 2201–2215. https://doi.org/10.1091/mbc.E13-02-0076

Berg, S., Kutra, D., Kroeger, T., Straehle, C.N., Kausler, B.X., Haubold, C., Schiegg, M., Ales, J., Beier, T., Rudy, M., Eren, K., Cervantes, J.I., Xu, B., Beuttenmueller, F., Wolny, A., Zhang, C., Koethe, U., Hamprecht, F.A., Kreshuk, A., 2019. ilastik: interactive machine learning for (bio)image analysis. Nat. Methods 16, 1226–1232. https://doi.org/10.1038/s41592-019-0582-9

Bondaz, A., Cirillo, L., Meraldi, P., Gotta, M., 2019. Cell polarity–dependent centrosome separation in the C. elegans embryo. J. Cell Biol. 218, 4112–4126. https://doi.org/10.1083/jcb.201902109

Bosveld, F., Markova, O., Guirao, B., Martin, C., Wang, Z., Pierre, A., Balakireva, M., Gaugue, I., Ainslie, A., Christophorou, N., Lubensky, D.K., Minc, N., Bellaïche, Y., 2016. Epithelial tricellular

junctions act as interphase cell shape sensors to orient mitosis. Nature 530, 495–498. https://doi.org/10.1038/nature16970

Buttrick, G.J., Beaumont, L.M.A., Leitch, J., Yau, C., Hughes, J.R., Wakefield, J.G., 2008. Akt regulates centrosome migration and spindle orientation in the early Drosophila melanogaster embryo. J. Cell Biol. 180, 537–548. https://doi.org/10.1083/jcb.200705085

Caballero-Mancebo, S., Gonzalez Suarez, D., Chenevert, J., McDougall, A., Turlier, H., Dumollard, R., 2026. Marine model organisms for mechanobiology studies, in: Evo-Devo: In Search of New Model Species, Results and Problems in Cell Differentiation. Springer-Nature.

Caballero-Mancebo, S., Shinde, R., Bolger-Munro, M., Peruzzo, M., Szep, G., Steccari, I., Labrousse-Arias, D., Zheden, V., Merrin, J., Callan-Jones, A., Voituriez, R., Heisenberg, C.-P., 2024. Friction forces determine cytoplasmic reorganization and shape changes of ascidian oocytes upon fertilization. Nat. Phys. 20, 310–321. https://doi.org/10.1038/s41567-023-02302-1

Carroll, M., Levasseur, M., Wood, C., Whitaker, M., Jones, K.T., McDougall, A., 2003. Exploring the mechanism of action of the sperm-triggered calcium-wave pacemaker in ascidian zygotes. J. Cell Sci. 116, 4997–5004. https://doi.org/10.1242/jcs.00846

Cheng, X., Ferrell, J.E., 2019. Spontaneous emergence of cell-like organization in Xenopus egg extracts. Science 366, 631–637. https://doi.org/10.1126/science.aav7793

Chiu, C.-L., Clack, N., the napari community, 2022. Napari: a Python Multi-Dimensional Image Viewer Platform for the Research Community. Microsc. Microanal. 28, 1576–1577. https://doi.org/10.1017/S1431927622006328

Costache, V., Hebras, C., Pruliere, G., Besnardeau, L., Failla, M., Copley, R.R., Burgess, D., Chenevert, J., McDougall, A., 2017. Kif2 localizes to a subdomain of cortical endoplasmic reticulum that drives asymmetric spindle position. Nat. Commun. 8, 917. https://doi.org/10.1038/s41467-017-01048-8

De Simone, A., Nédélec, F., Gönczy, P., 2016. Dynein Transmits Polarized Actomyosin Cortical Flows to Promote Centrosome Separation. Cell Rep. 14, 2250–2262. https://doi.org/10.1016/j.celrep.2016.01.077

Dumollard, R., Minc, N., Salez, G., Aicha, S.B., Bekkouche, F., Hebras, C., Besnardeau, L., McDougall, A., 2017. The invariant cleavage pattern displayed by ascidian embryos depends on spindle positioning along the cell's longest axis in the apical plane and relies on asynchronous cell divisions. eLife 6, e19290. https://doi.org/10.7554/eLife.19290

Fujii, K., Kondo, T., Kimura, A., 2023. Enucleation of the C. elegans embryo revealed dynein-dependent spacing between microtubule asters. Life Sci. Alliance 7, e202302427. https://doi.org/10.26508/lsa.202302427

Giammona, J., Campàs, O., 2021. Physical constraints on early blastomere packings. PLOS Comput. Biol. 17, e1007994. https://doi.org/10.1371/journal.pcbi.1007994

Godard, B.G., Dumollard, R., Heisenberg, C.-P., McDougall, A., 2021. Combined effect of cell geometry and polarity domains determines the orientation of unequal division. eLife 10, e75639. https://doi.org/10.7554/eLife.75639

Gönczy, P., Grill, S., Stelzer, E.H., Kirkham, M., Hyman, A.A., 2001. Spindle positioning during the asymmetric first cell division of Caenorhabditis elegans embryos. Novartis Found. Symp. 237, 164–175; discussion 176-181. https://doi.org/10.1002/0470846666.ch13

Grill, S.W., Gönczy, P., Stelzer, E.H., Hyman, A.A., 2001. Polarity controls forces governing asymmetric spindle positioning in the Caenorhabditis elegans embryo. Nature 409, 630–633. https://doi.org/10.1038/35054572

Grill, S.W., Hyman, A.A., 2005. Spindle Positioning by Cortical Pulling Forces. Dev. Cell 8, 461–465. https://doi.org/10.1016/j.devcel.2005.03.014

Hertwig, O., 1884. Das Problem der Befruchtung und der Isotropie des Eies: eine Theorie der Vererbung. Verlag von Gustav Fischer.

Kamath, K., Okouneva, T., Larson, G., Panda, D., Wilson, L., Jordan, M.A., 2006. 2-Methoxyestradiol suppresses microtubule dynamics and arrests mitosis without depolymerizing microtubules. Mol. Cancer Ther. 5, 2225–2233. https://doi.org/10.1158/1535-7163.MCT-06-0113

899 Kelkar, M., Bohec, P., Smith, M.B., Sreenivasan, V., Lisica, A., Valon, L., Ferber, E., Baum, B., Salbreux,
900 G., Charras, G., 2022. Spindle reorientation in response to mechanical stress is an emergent
901 property of the spindle positioning mechanisms. Proc. Natl. Acad. Sci. 119, e2121868119.
902 https://doi.org/10.1073/pnas.2121868119
903 Kimura, K., Kimura, A., 2011a. A novel mechanism of microtubule length-dependent force to pull
904 centrosomes toward the cell center. BioArchitecture 1, 74–79.
905 https://doi.org/10.4161/bioa.1.2.15549
906 Kimura, K., Kimura, A., 2011b. Intracellular organelles mediate cytoplasmic pulling force for
907 centrosome centration in the Caenorhabditis elegans early embryo. Proc. Natl. Acad. Sci. U. S.
908 A. 108, 137–142. https://doi.org/10.1073/pnas.1013275108
909 Kiyomitsu, T., 2019. The cortical force-generating machinery: how cortical spindle-pulling forces are
910 generated. Curr. Opin. Cell Biol., Cell Dynamics 60, 1–8.
911 https://doi.org/10.1016/j.ceb.2019.03.001
912 Laan, L., Pavin, N., Husson, J., Romet-Lemonne, G., van Duijn, M., López, M.P., Vale, R.D., Jülicher, F.,
913 Reck-Peterson, S.L., Dogterom, M., 2012. Cortical Dynein Controls Microtubule Dynamics to
914 Generate Pulling Forces that Reliably Position Microtubule Asters. Cell 148, 502–514.
915 https://doi.org/10.1016/j.cell.2012.01.007
916 Lane, J.D., Allan, V.J., 1999. Microtubule-based Endoplasmic Reticulum Motility in Xenopus laevis:
917 Activation of Membrane-associated Kinesin during Development. Mol. Biol. Cell 10, 1909–
918 1922. https://doi.org/10.1091/mbc.10.6.1909
919 McDougall, A., Chenevert, J., Godard, B.G., Dumollard, R., 2019. Emergence of Embryo Shape During
920 Cleavage Divisions, in: Tworzydlo, W., Bilinski, S.M. (Eds.), Evo-Devo: Non-Model Species in Cell
921 and Developmental Biology, Results and Problems in Cell Differentiation. Springer
922 International Publishing, Cham, pp. 127–154. https://doi.org/10.1007/978-3-030-23459-1_6
923 McDougall, A., Lee, K.W.-M., Dumollard, R., 2014. Microinjection and 4D fluorescence imaging in the
924 eggs and embryos of the ascidian Phallusia mammillata. Methods Mol. Biol. Clifton NJ 1128,
925 175–185. https://doi.org/10.1007/978-1-62703-974-1_11
926 Meijering, E., Dzyubachyk, O., Smal, I., 2012. Methods for Cell and Particle Tracking, in: Methods in
927 Enzymology. Elsevier, pp. 183–200. https://doi.org/10.1016/B978-0-12-391857-4.00009-4
928 Meyerzon, M., Gao, Z., Liu, J., Wu, J.-C., Malone, C.J., Starr, D.A., 2009. Centrosome attachment to the
929 C. elegans male pronucleus is dependent on the surface area of the nuclear envelope. Dev.
930 Biol. 327, 433–446. https://doi.org/10.1016/j.ydbio.2008.12.030
931 Middelkoop, T.C., Neipel, J., Cornell, C.E., Naumann, R., Pimpale, L.G., Jülicher, F., Grill, S.W., 2024. A
932 cytokinetic ring-driven cell rotation achieves Hertwig's rule in early development. Proc. Natl.
933 Acad. Sci. 121, e2318838121. https://doi.org/10.1073/pnas.2318838121
934 Minc, N., Burgess, D., Chang, F., 2011. Influence of Cell Geometry on Division-Plane Positioning. Cell
935 144, 414–426. https://doi.org/10.1016/j.cell.2011.01.016
936 Minc, N., Piel, M., 2012. Predicting division plane position and orientation. Trends Cell Biol. 22, 193–
937 200. https://doi.org/10.1016/j.tcb.2012.01.003
938 Mukherjee, R.N., Sallé, J., Dmitrieff, S., Nelson, K.M., Oakey, J., Minc, N., Levy, D.L., 2020. The
939 Perinuclear ER Scales Nuclear Size Independently of Cell Size in Early Embryos. Dev. Cell 54,
940 395-409.e7. https://doi.org/10.1016/j.devcel.2020.05.003
941 Negishi, T., Takada, T., Kawai, N., Nishida, H., 2007. Localized PEM mRNA and Protein Are Involved in
942 Cleavage-Plane Orientation and Unequal Cell Divisions in Ascidians. Curr. Biol. 17, 1014–1025.
943 https://doi.org/10.1016/j.cub.2007.05.047
944 Omer, S., Greenberg, S.R., Lee, W.-L., 2018. Cortical dynein pulling mechanism is regulated by
945 differentially targeted attachment molecule Num1. eLife 7, e36745.
946 https://doi.org/10.7554/eLife.36745
947 Pierre, A., Sallé, J., Wühr, M., Minc, N., 2016a. Generic Theoretical Models to Predict Division Patterns
948 of Cleaving Embryos. Dev. Cell 39, 667–682. https://doi.org/10.1016/j.devcel.2016.11.018

Prodon, F., Chenevert, J., Hébras, C., Dumollard, R., Faure, E., Gonzalez-Garcia, J., Nishida, H., Sardet, C., McDougall, A., 2010. Dual mechanism controls asymmetric spindle position in ascidian germ cell precursors. Development 137, 2011–2021. https://doi.org/10.1242/dev.047845

Redemann, S., Pecreaux, J., Goehring, N.W., Khairy, K., Stelzer, E.H.K., Hyman, A.A., Howard, J., 2010. Membrane Invaginations Reveal Cortical Sites that Pull on Mitotic Spindles in One-Cell C. elegans Embryos. PLOS ONE 5, e12301. https://doi.org/10.1371/journal.pone.0012301

Rosfelter, A., de Labbey, G., Chenevert, J., Dumollard, R., Schaub, S., Machaty, Z., Besnardeau, L., Gonzalez Suarez, D., Hebras, C., Turlier, H., Burgess, D.R., McDougall, A., 2024. Reduction of cortical pulling at mitotic entry facilitates aster centration. J. Cell Sci. 137, jcs262037. https://doi.org/10.1242/jcs.262037

Roure, A., Rothbächer, U., Robin, F., Kalmar, E., Ferone, G., Lamy, C., Missero, C., Mueller, F., Lemaire, P., 2007. A Multicassette Gateway Vector Set for High Throughput and Comparative Analyses in Ciona and Vertebrate Embryos. PLOS ONE 2, e916. https://doi.org/10.1371/journal.pone.0000916

Sachs, J., 1877. Über die Anordnung der Zellen in jüngsten Pflanzentheilen. Druck und Verlag der Stahel'schen Buch- & Kunsthandlung.

Sardet, C., McDougall, A., Yasuo, H., Chenevert, J., Pruliere, G., Dumollard, R., Hudson, C., Hebras, C., Le Nguyen, N., Paix, A., 2011. Embryological Methods in Ascidians: The Villefranche-sur-Mer Protocols, in: Pelegri, F.J. (Ed.), Vertebrate Embryogenesis: Embryological, Cellular, and Genetic Methods, Methods in Molecular Biology. Humana Press, Totowa, NJ, pp. 365–400. https://doi.org/10.1007/978-1-61779-210-6_14

Schindelin, J., Arganda-Carreras, I., Frise, E., Kaynig, V., Longair, M., Pietzsch, T., Preibisch, S., Rueden, C., Saalfeld, S., Schmid, B., Tinevez, J.-Y., White, D.J., Hartenstein, V., Eliceiri, K., Tomancak, P., Cardona, A., 2012. Fiji: an open-source platform for biological-image analysis. Nat. Methods 9, 676–682. https://doi.org/10.1038/nmeth.2019

Schulze, J., Schierenberg, E., 2011. Evolution of embryonic development in nematodes. EvoDevo 2, 18. https://doi.org/10.1186/2041-9139-2-18

Seirin-Lee, S., Yamamoto, K., Kimura, A., 2022. The extra-embryonic space and the local contour are crucial geometric constraints regulating cell arrangement. Development 149, dev200401. https://doi.org/10.1242/dev.200401

Shamipour, S., Caballero-Mancebo, S., Heisenberg, C.-P., 2021. Cytoplasm's Got Moves. Dev. Cell 56, 213–226. https://doi.org/10.1016/j.devcel.2020.12.002

Stoev, I.D., Bolger-Munro, M., Minopoli, A., Wagner, S., Krishnaswamy, V.R., Erben, E., Weißenbruch, K., Maghelli, N., Bastmeyer, M., Heisenberg, C.-P., Kreysing, M., 2025. Active and Probe-Free Intracellular Rheology via Phase-Sensitive Thermoviscous Flows. https://doi.org/10.1101/2025.04.07.647540

Stringer, C., Wang, T., Michaelos, M., Pachitariu, M., 2021. Cellpose: a generalist algorithm for cellular segmentation. Nat. Methods 18, 100–106. https://doi.org/10.1038/s41592-020-01018-x

Tanenbaum, M.E., Medema, R.H., 2010. Mechanisms of Centrosome Separation and Bipolar Spindle Assembly. Dev. Cell 19, 797–806. https://doi.org/10.1016/j.devcel.2010.11.011

Thevenaz, P., Ruttimann, U.E., Unser, M., 1998. A pyramid approach to subpixel registration based on intensity. IEEE Trans. Image Process. 7, 27–41. https://doi.org/10.1109/83.650848

Wong, S.-S., Wainman, A., Saurya, S., Raff, J.W., 2024. Regulation of centrosome size by the cell-cycle oscillator in Drosophila embryos. EMBO J. 43, 414–436. https://doi.org/10.1038/s44318-023-00022-z

Woźniak, M.J., Bola, B., Brownhill, K., Yang, Y.-C., Levakova, V., Allan, V.J., 2009. Role of kinesin-1 and cytoplasmic dynein in endoplasmic reticulum movement in VERO cells. J. Cell Sci. 122, 1979–1989. https://doi.org/10.1242/jcs.041962

Wu, H.-Y., Kabacaoğlu, G., Nazockdast, E., Chang, H.-C., Shelley, M.J., Needleman, D.J., 2024. Laser ablation and fluid flows reveal the mechanism behind spindle and centrosome positioning. Nat. Phys. 20, 157–168. https://doi.org/10.1038/s41567-023-02223-z

Wühr, M., Tan, E.S., Parker, S.K., Detrich, H.W., Mitchison, T.J., 2010. A model for cleavage plane determination in early amphibian and fish embryos. Curr. Biol. CB 20, 2040–2045. https://doi.org/10.1016/j.cub.2010.10.024

Xie, J., Najafi, J., Le Borgne, R., Verbavatz, J.-M., Durieu, C., Sallé, J., Minc, N., 2022. Contribution of cytoplasm viscoelastic properties to mitotic spindle positioning. Proc. Natl. Acad. Sci. 119, e2115593119. https://doi.org/10.1073/pnas.2115593119

SUPPLEMENTAL FIGURES

Supplemental Figure 1

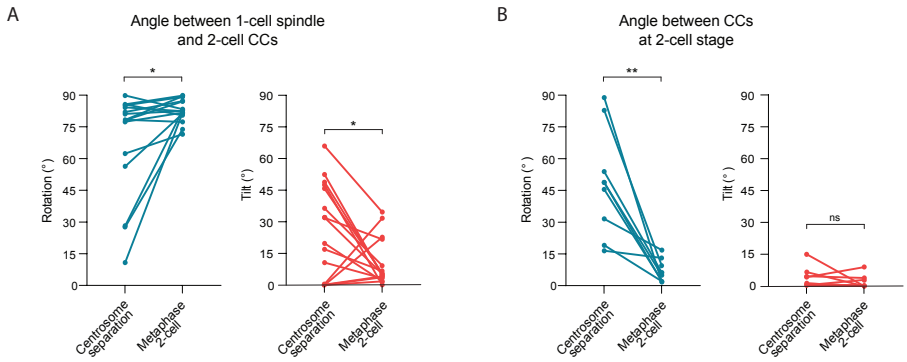

Figure S1: CCs of sister cells become parallel and coplanar at the 2-cell stage (relative to Fig. 1).
(A) Plot of the initial (Centrosome separation) and final (Metaphase 2-cell) rotation (left) and tilt (right) angles between the 2-cell stage CCs or spindles and the 1-cell stage spindle (*N* = 9 embryos, *n* = 18 cells; rotation: paired Wilcoxon test, *P=0.0131; tilt: paired Wilcoxon test, *P=0.0250).
(B) Plot of the initial (Centrosome separation) and final (Metaphase 2-cell) rotation (left) and tilt (right) angles between the left and right CCs or spindles at 2-cell stage (*N* = 9 embryos; rotation: paired t test, **P=0.0017; tilt: paired Wilcoxon test, ns – not significant).

Supplemental Figure 2

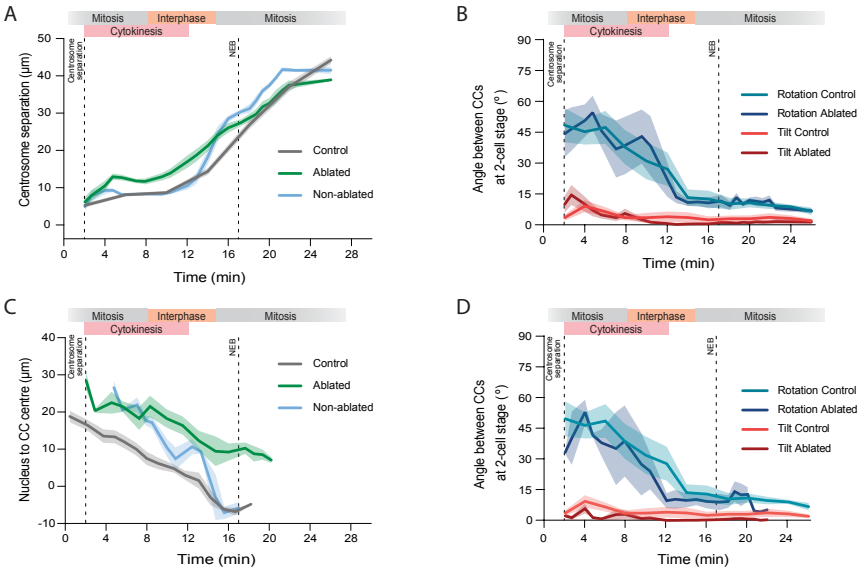

Figure S2: Centrosome migration and alignment in laser-ablated embryos (relative to Fig. 2).
(A) Plot of the separation of centrosomes within a CC as a function of time in control embryos (grey; *N* = 9 embryos, *n* = 18 cells), ablated cell (green; *N* = 5 embryos, *n* = 5 cells), and non-ablated cell (blue; *N* = 5 embryos, *n* = 5 cells) of laser-ablated embryos between the centrosomes. The dashed line at 17 min indicates NEB. Error bars, standard error of the mean.
(B) Plot of the rotation and tilt angles between the CCs or the spindles of the left and right cells at the 2-cell stage as a function of time in control (*N* = 9 embryos) and in ablated embryos between the centrosomes in one cell (*N* = 5 embryos. The dashed line at 17 min indicates NEB. Error bars, standard error of the mean.
(C) Plot of the distance between the edge of the nucleus and the entre of the CC as a function of time in control embryos (grey; *N* = 6 embryos, *n* = 12 cells), ablated cell (green; *N* = 4 embryos, *n* = 4 cells), and non-ablated cell (blue; *N* = 4 embryos, *n* = 4 cells) of laser-ablated embryos between the centrosomes and the nucleus. The dashed line at 17 min indicates NEB. Error bars, standard error of the mean.
(D) Plot of the rotation and tilt angles between the CCs or the spindles of the left and right cells at the 2-cell stage as a function of time in control (*N* = 9 embryos) and ablated embryos between the centrosomes and the nucleus in one cell (*N* = 4 embryos). The dashed line at 17 min indicates NEB. Error bars, standard error of the mean.

Supplemental Figure 3

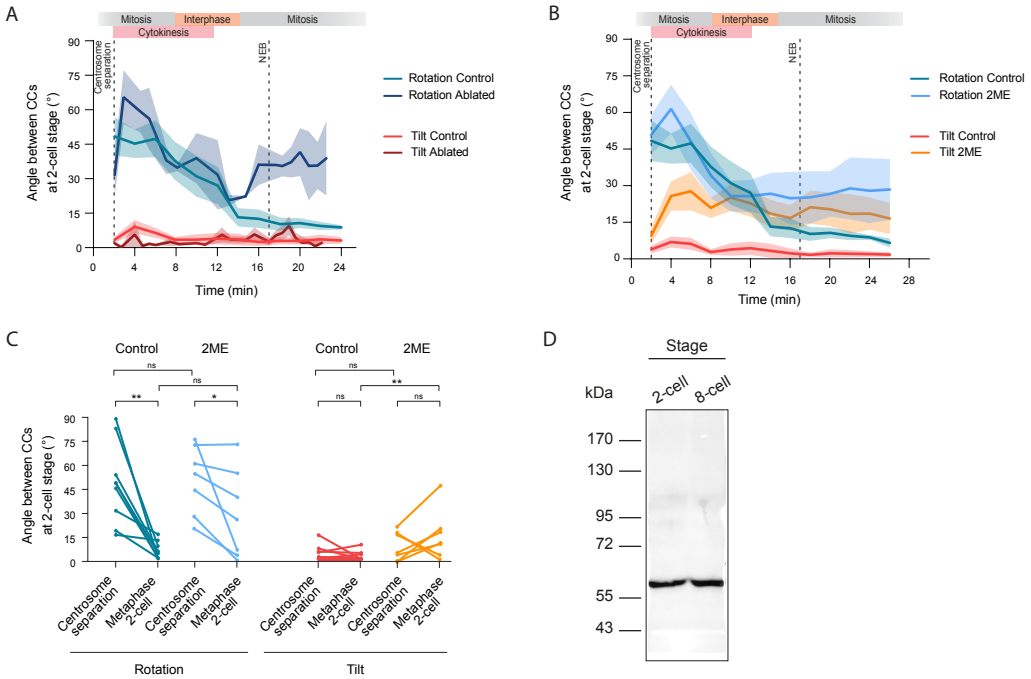

Figure S3: Centrosome alignment relies on forces generated along astral microtubules (relative to Fig. 3).

(A) Plot of the rotation and tilt angles between the CCs or the spindles of the left and right cells at the 2-cell stage as a function of time in control embryos (*N* = 9 embryos), ablated cell (*N* = 4 embryos, *n* = 4 cells), and non-ablated cell (*N* = 4 embryos, *n* = 4 cells) of laser-ablated embryos. The dashed line at 17 min indicates NEB. Error bars, standard error of the mean.

(B) Plot of the rotation and tilt angles between the CCs or the spindles of the left and right cells at the 2-cell stage as a function of time in control (*N* = 9 embryos) and 2-methoxyestradiol (2ME)-treated (*N* = 7 embryos). The dashed line at 17 min indicates NEB. Error bars, standard error of the mean.

(B') Plot of the initial (Centrosome separation) and final (Metaphase 2-cell) rotation (left) and tilt (right) angles between the left and right CCs or spindles at 2-cell stage in control embryos (*N* = 9 embryos; rotation: paired Wilcoxon test, *P=0.0131; tilt: paired Wilcoxon test, *P=0.0250) and embryos treated with 2ME (*N* = 7 embryos; rotation: paired t test (*P=0.0462); tilt: paired t test (ns – not significant)). Control vs. 2ME rotation angle: one-way ANOVA (***P=0.0005) with Šídák's multiple comparisons test (ns – not significant). Control vs. 2ME tilt angle: Kruskal-Wallis test (*P=0.0186) with Dunn's multiple comparisons test (ns – not significant, **P=0.0040).

(C) Western blot of extracts of *Phallusia mammillata* 2- and 8-cell stage embryos probed with anti-dynactin antibody.

Supplemental Figure 4

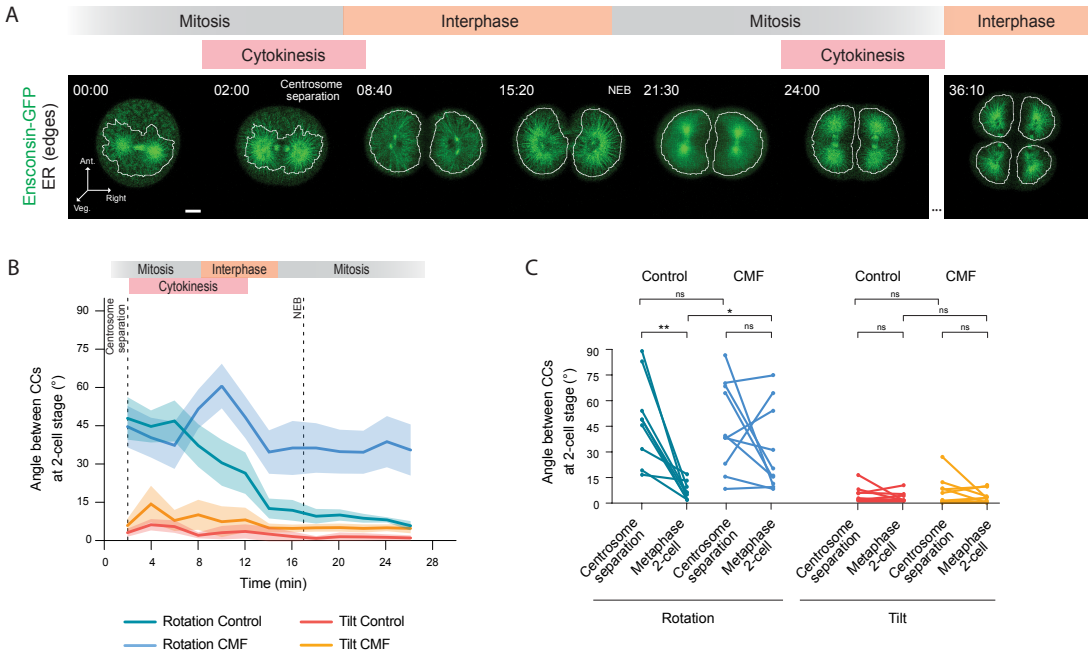

Figure S4: Cytoplasmic pulling controls rotation angles (relative to Fig. 4).

(A) Maximum intensity projections of confocal fluorescent images of microtubules (green) and the edges of the ER accumulation around spindles (white) in an ascidian embryo from 1-cell stage metaphase to 4-cell stage interphase. Ant. is anterior, Veg. is vegetal, and NEB is nuclear envelope breakdown. Time is in minutes:seconds. Scale bar, 30 µm.

(B) Plot of the rotation and tilt angles between the CCs or the spindles of the left and right cells at the 2-cell stage as a function of time in control (*N* = 9 embryos) and in calcium and magnesium-free seawater (CMF)-treated embryos (*N* = 10 embryos). The dashed line at 17 min indicates NEB. Error bars, standard error of the mean.

(C) Plot of the initial (Centrosome separation) and final (Metaphase 2-cell) rotation (left) and tilt (right) angles between the left and right CCs or spindles at 2-cell stage in control embryos (*N* = 9 embryos; rotation: paired Wilcoxon test, *P=0.0131; tilt: paired Wilcoxon test, *P=0.0250) and CMF-treated embryos (*N* = 10 embryos; rotation: paired t test, ns - not significant; tilt: paired t test, ns – not significant). Control vs. CMF rotation angle: one-way ANOVA (***P=0.0010) with Šídák's multiple comparisons test (ns – not significant, *P=0.0431). Control vs. CMF tilt angle: Kruskal-Wallis (ns – not significant) with Dunn's multiple comparisons test ns – not significant).

Supplemental Figure 5

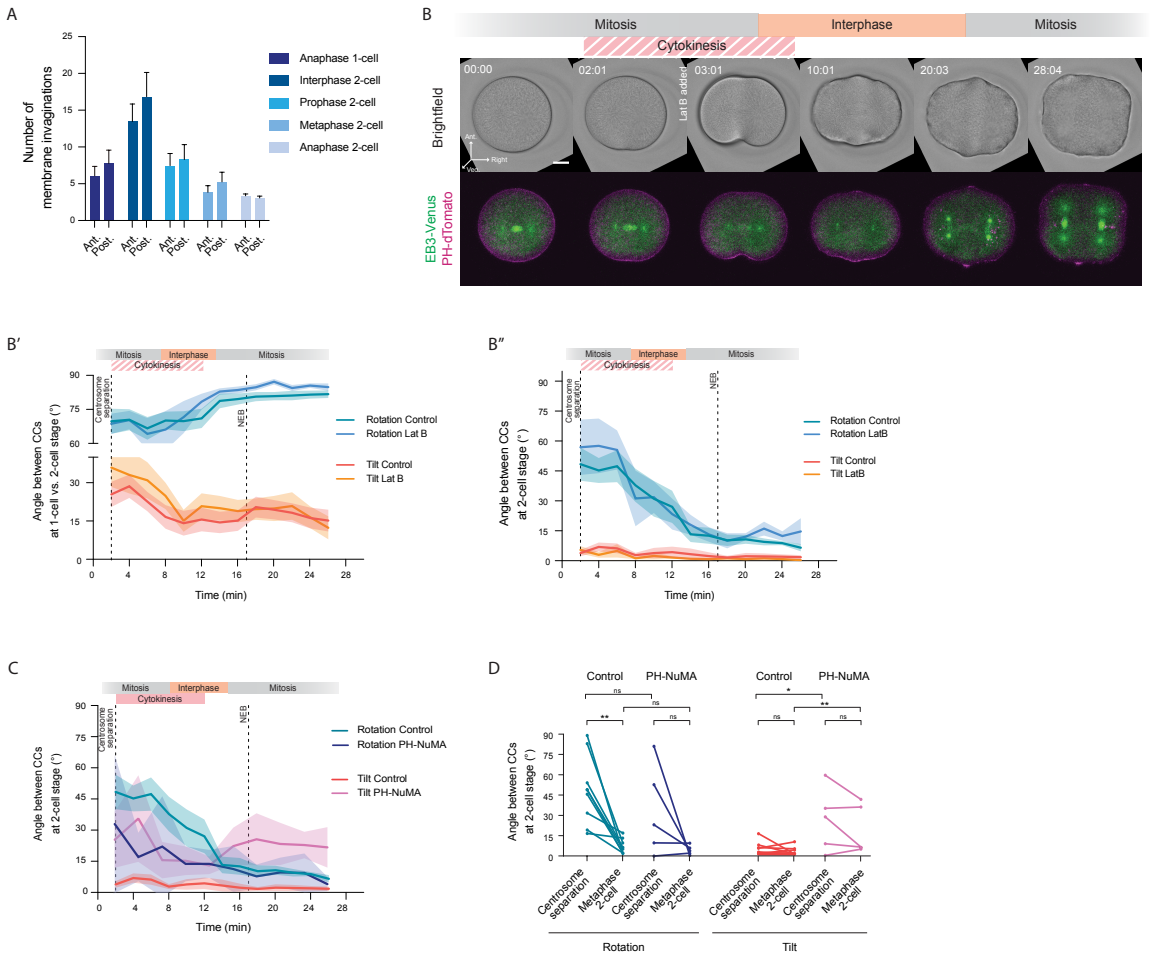

Figure S5: Cortical pulling is increased in the posterior of the ascidian 2-cell stage embryo (relative to Fig. 5).

(A) Bar plot of the average number of membrane invaginations at the anterior (Ant.) and posterior (Post.) sides of the embryo as a function of the cell cycle stage. Data is taken from Fig. 5B'.

(B) Brightfield and confocal fluorescent images of a central z-slice of the plasma membrane (magenta), and maximum intensity projections of centrosomes (green) in an ascidian embryo from 1-cell stage metaphase to 2-cell stage metaphase treated with 1 µg/ml Latrunculin B at 1-cell stage anaphase. Ant. is anterior, Veg. is vegetal. Time is in minutes:seconds. Scale bar, 30 µm.

(B') Plot of the rotation and tilt angles between the CCs or the spindles at the 2-cell stage and the spindle at the 1-cell stage as a function of time in control embryos (*N* = 9 embryos, *n* = 18 cells) and Latrunculin B-treated embryos (*N* = 5 embryos, *n* = 10 cells). The dashed line at 17 min indicates NEB. Error bars, standard error of the mean.

(B'') Plot of the rotation and tilt angles between the CCs or the spindles of the left and right cells at the 2-cell stage as a function of time in control (*N* = 9 embryos) and Latrunculin B-treated (*N* = 5 embryos). The dashed line at 17 min indicates NEB. Error bars, standard error of the mean.

(C) Plot of the rotation and tilt angles between the CCs or the spindles of the left and right cells at the 2-cell stage as a function of time in control (*N* = 9 embryos) and embryos expressing PH-NuMA (*N* = 5 embryos, *n* = 10 cells). The dashed line at 17 min indicates NEB. Error bars, standard error of the mean. **(D)** Plot of the initial (Centrosome separation) and final (Metaphase 2-cell) rotation (left) and tilt (right) angles between the left and right CCs or spindles at 2-cell stage in control embryos (*N* = 9 embryos; rotation: paired Wilcoxon test, *P=0.0131; tilt: paired Wilcoxon test, *P=0.0250) and embryos overexpressing PH-NuMA (*N* = 5 embryos; rotation: paired t test, ns - not significant; tilt: Wilcoxon test, ns – not significant). Control vs. PH-NuMA rotation angle: one-way ANOVA (***P=0.0005) with Šídák's multiple comparisons test (ns – not significant). Control vs. PH-NuMA tilt angle: Kruskal-Wallis test (*P=0.0210) with Dunn's multiple comparisons test (*P=0.0146, ns – not significant).

MOVIE LEGENDS

Movie 1. Centrosomal complex orientation during the first two cleavages in ascidian embryos, related to Fig. 1 and S1. Time-lapse brightfield (left panel) and fluorescent confocal video of a representative ascidian embryo injected with PH-dTomato mRNA (magenta, right panel) and EB3-3xVenus mRNA (green, right panel) to mark membrane and centrosomes, respectively. Time is in minutes:seconds. Time interval, 2 min.

Movie 2. Centrosome and nucleus migration during interphase of the 2-cell stage in ascidian embryos, related to Fig. 2. Time-lapse fluorescent confocal video of a representative ascidian embryo injected with EB3-mScarlet mRNA (green), H2B-Venus mRNA (magenta) to mark centrosomes and the DNA, respectively, and incubated in MitoTracker™ Deep Red (cyan) to label the mitochondria. Time is in minutes:seconds. Time interval, 16 s.

Movie 3. Laser ablation of intercentrosomal microtubules during CC migration at the 2-cell stage of ascidian embryos, related to Fig. 2 and S2. Time-lapse fluorescent confocal video of a representative ascidian embryo injected with EB3-mScarlet mRNA (magenta) and Ensconsin-3xGFP mRNA (green) to mark centrosomes and microtubules, respectively. The ablation site is indicated by the arrowhead. Time is in minutes:seconds. Time interval, 12.8 s.

Movie 4. Laser ablation of microtubules between the CC and the nucleus during CC migration at the 2-cell stage of ascidian embryos, related to Fig. 2 and S2. Time-lapse fluorescent confocal video of a representative ascidian embryo injected with H2B-Venus mRNA (magenta) and Ensconsin-dTomato mRNA (green) to mark DNA and microtubules, respectively. The ablation site is indicated by the arrowheaad. Time is in minutes:seconds. Time interval, 12.8 s.

Movie 5. Laser ablation of astral microtubules during CC migration at the 2-cell stage of ascidian embryos, related to Fig. 3 and S3. Time-lapse fluorescent confocal video of a representative ascidian embryo injected with EB3-mScarlet mRNA (magenta) and Ensconsin-3xGFP mRNA (green) to mark centrosomes and microtubules, respectively. The ablation site is indicated by the arrowhead. Time is in minutes:seconds. Time interval, 12.8 s.

1234

1235 **Movie 6.** Endoplasmic reticulum rearrangement during the first two cleavages in ascidian embryos,
1236 related to Fig. 4 and S4. Time-lapse fluorescent confocal video of a representative ascidian embryo
1237 injected with PH-dTomato mRNA (magenta) and Reticulon-Venus mRNA (grey) to mark the membrane
1238 and endoplasmic reticulum, respectively. Time is in minutes:seconds. Time interval, 110 s.
1239

1240 **Movie 7.** Centrosomal complex orientation during the first two cleavages in ascidian embryos cultured
1241 in calcium and magnesium-free seawater, related to Fig. 4 and S4. Time-lapse brightfield (left panel)
1242 and fluorescent confocal video of a representative ascidian embryo injected with PH-dTomato mRNA
1243 (magenta, right panel) and EB3-3xVenus mRNA (green, right panel) to mark membrane and
1244 centrosomes, respectively. Time is in minutes:seconds. Time interval, 2 min.
1245

1246 **Movie 8.** Cortical pulling assay in control ascidian embryos, related to Fig. 5 and S5. Time-lapse
1247 fluorescent confocal video of a representative ascidian embryo treated with 1μg/ml Latrunculin B and
1248 injected with H2B-Venus mRNA (magenta) to mark the DNA, and incubated in CellMask^{TM} Orange to
1249 label the plasma membrane (grey). Time is in minutes:seconds. Time interval, 20 s.
1250

1251 **Movie 9.** Cortical pulling assay in ascidian embryos expressing PH-NuMA, related to Fig. 5 and S5. Time-
1252 lapse fluorescent confocal video of a representative ascidian embryo treated with 1μg/ml Latrunculin
1253 B and incubated in CellMask^{TM} Orange to label the plasma membrane (grey, left panel) and injected
1254 with PH-NuMA-Venus mRNA (magenta, right panel) to mark exogenous cortical NuMA. Time is in
1255 minutes:seconds. Time interval, 16 s.
1256

1257 **Movie 10.** Centrosomal complex orientation during the first two cleavages in ascidian embryos
1258 expressing PH-NuMA to increase cortical pulling, related to Fig. 5 and S5. Time-lapse brightfield (left
1259 panel) and fluorescent confocal video of a representative ascidian embryo injected with PH-NuMA-
1260 Venus mRNA (magenta, right panel) and EB3-mScarlet (green, right panel) to mark exogenous cortical
1261 NuMA and centrosomes, respectively. Time is in minutes:seconds. Time interval, 2 min.
1262